



TRABAJO FIN DE MÁSTER
MASTER'S THESIS

Gamma-Ray Spectra from Young Stellar Clusters: A Simulation-Based Approach

By
José María García Morillo

For the programme
Master en Física y Matemáticas (FisyMat)

Supervised by
Rubén López Coto and Stefano Menchiari

As a member of
VHEGA Group - Instituto de Astrofísica de Andalucía (CSIC)

Academic year 2024/25

Declaración de originalidad

D. José María García Morillo, con DNI 77937226R, garantiza con su firma que en la realización del TFM de título *Gamma-Ray Spectra from Young Stellar Clusters: A Simulation-Based Approach* se han respetado los derechos de otros autores a ser citados cuando se han utilizado sus resultados o publicaciones.



Firmado: José María García Morillo
En Granada a 30 de junio de 2025.

Contents

Introduction	1
1 Cosmic rays acceleration in star clusters	3
1.1 Galactic cosmic ray acceleration	3
1.2 Introduction to stellar clusters physics	6
1.3 The transport equation	10
2 Simulating stellar clusters with PLUTO	13
2.1 What is PLUTO?	13
2.2 Configurations considered	15
2.3 Results	18
2.3.1 Purely hydrodynamical system	18
2.3.2 Thermal conduction	21
2.3.3 Radiative cooling	25
2.3.4 Application to real star cluster	28
3 Development of a numerical solver for transport equation	31
3.1 Mathematical foundations of the solver	31
3.1.1 Diffusion operator	34
3.1.2 Loss operator	37
3.1.3 Advection operator	38
3.2 Numerical validations of the solver	41
3.2.1 Diffusion routine	41
3.2.2 Loss routine	42
3.2.3 Advection routine	43
Conclusions	46
Bibliography	48

Introduction

In recent decades, high-energy astrophysics has undergone a remarkable transformation driven by advances in our observational, computational and theoretical modelling capabilities. One of the fields that has benefited most from these advances is the study of young star clusters; objects that, in addition to their traditional interest as natural laboratories for stellar evolution, gravitational dynamics and galactic formation [1, 2, 3, 4, 5, 6], have emerged as possible cosmic ray accelerators. This possibility has opened up to new interdisciplinary studies connecting stellar evolution, plasma physics and particle physics, greatly enriching the state of the art of modern astrophysics.

A central open question in astroparticle physics is the origin of cosmic rays with energies reaching the PeV scale. While supernova remnants have long been considered the primary galactic accelerators [7, 8, 9, 10, 11], recent observational and theoretical studies suggest they may fall short of explaining the CR spectrum up to a few PeV [12], as particles can only be accelerated up to a few hundreds of TeV. This has led to the search for so-called *PeVatrons* (astrophysical sources capable of accelerating particles to PeV energies).

In this context, young massive star clusters have recently gained attention as promising candidates [13, 14], as they concentrate a large number of massive stars in relatively small volumes, giving rise to extreme physical conditions. The powerful stellar winds generated by these stars can interact with each other, forming hot bubbles of ionised gas and turbulent shocks that could act as efficient sources of particle acceleration [15, 16, 17, 18, 19, 20, 21, 13, 22, 23]. Their collective winds, high densities and turbulent environments provide the necessary conditions for long-term particle acceleration through repeated shock interactions or stochastic processes. Thus, the hypothesis that these environments may contribute significantly to the galactic cosmic ray population has become increasingly relevant, especially given the limitations of supernova remnants in explaining all the features of the observed spectrum. However, many aspects of this scenario remain

unexplored or poorly constrained, both theoretically and observationally. The present project contributes to this emerging field by providing a computational framework to simulate these environments and test their viability as potential PeVatrons.

This work presents a numerical study of the environment generated by the collective stellar wind in young clusters, with the aim of analysing its structural properties and studying the propagation of particles within it. The idea behind this work has been to always stick to one dimensional models, so that their computational workload is light enough to make possible eventual systematic analysis and fits for the interpretation of the observed γ -ray emission detected in several galactic clusters. To this end, a complete numerical solver for the spherically symmetric transport equation has been developed as part of this work. To the best of the author's knowledge, no existing public tool is specifically designed to address this problem. Cosmic ray transport is typically studied on galactic scales, and the available codes (such as GALPROP [24], DRAGON [25] or PICARD [26]) are tailored for different geometries, usually Cartesian or cylindrical, not supporting spherical symmetry. This constitutes a major contribution to the field, providing a tool specifically adapted to the study of astrophysical sources.

The work is structured as follows. First, the necessary theoretical framework is introduced, describing the physics underlying the interaction of the stellar wind, the fundamentals of cosmic ray propagation and the transport model used. Next, the methodology used in the stellar bubble simulations with PLUTO is described, detailing the domain design, the initial and boundary conditions and the main results obtained in the form of spatial profiles of density, pressure, velocity and temperature. Subsequently, the numerical solver developed for this project is presented, explaining its mathematical formulation, the discretisation strategy and the algorithms used. A subsection of numerical validation is included. Finally, a conclusion summarizes the main findings and outlines the future work required to integrate the solver with the hydrodynamical simulations, ultimately enabling a complete modelling pipeline for studying observable cosmic ray emission from stellar clusters.

This approach is intended to be a first step towards the construction of a computational tool that allows realistic simulations of star clusters to be connected with γ -ray observations. In addition to contributing to the understanding of the role of these objects in particle acceleration, the development of a simulation and analysis tools constitutes a methodological added value, expanding the capabilities of numerical research in high-energy astrophysics.

Chapter 1

Cosmic rays acceleration in star clusters

1.1 Galactic cosmic ray acceleration

Cosmic rays (CRs) were discovered in the early XXth century, usually attributed to the Austrian physicist Victor Hess, who conducted a series of balloon flights to measure atmospheric ionization between 1911 and 1913. At the time, it was believed that radiation in the atmosphere came from the Earth's crust, but Hess found that ionization rate actually increased with altitude, suggesting an extraterrestrial origin. A key ascent during a solar eclipse confirmed the Sun was not the source, leading Hess to conclude that highly penetrating radiation was entering the atmosphere from space. His pioneering work earned him the Nobel Prize in Physics in 1936, cementing his role as the discoverer of CRs.

It is also worth mentioning the work of Italian physicist Domenico Pacini, who, prior to Hess's flights, conducted underwater measurements that revealed a significant decrease in radiation compared to the surface, thus suggesting a non-terrestrial component. Though his work has been historically overlooked, Pacini's contribution is now recognized as a foundational piece in the discovery of CRs [27].

Since the discovery of CRs, extensive research has been conducted to understand their nature, origin and impact in the Universe. We now know that CRs are predominantly composed of atomic nuclei (about 99%) with protons making up approximately 87% and alpha particles around 12%, along with a smaller contribution from heavier nuclei and minor fraction of electrons and antimatter [28]. Far from being a mere curiosity of high-energy astrophysics, CRs are now

recognized as a fundamental component of the Universe. In the Milky Way, their energy density is estimated to be $U_{\text{CR}} \approx 1 \text{ eV cm}^{-3}$ [29], comparable to that of other key constituents such as the interstellar radiation field ($\sim 0.5 \text{ eV cm}^{-3}$; [30]), the average Galactic magnetic field ($\sim 0.22 \text{ eV cm}^{-3}$; [29]) and the cosmic microwave background ($\sim 0.26 \text{ eV cm}^{-3}$; [31]). This energetic presence makes CRs essential not only in the context of high-energy phenomena, but also in the dynamics of the interstellar medium and the process of star formation, where thanks to their ability to penetrate deep within diffuse and molecular clouds, they can provide significant ionization, ultimately affecting the dynamic of the cloud and triggering numerous chemical reactions creating complex molecular compounds.

However, despite over a century of research, many open questions remain regarding the nature and origin of CRs. One of the most important enigmas relates to the structure of the observed energy spectrum. The CR spectrum measured at Earth is well described by a broken power law extending across nearly 12 decades in energy. Above approximately 10 GeV, the spectral index starts around about -2.7 , but the spectrum exhibits three notable features: the so-called *knee* at $\sim 3 \cdot 10^{15} \text{ eV}$, the *ankle* at $\sim 10^{18.5} \text{ eV}$, and a suppression at the highest energies [32]. Between the knee and the ankle the spectral index slightly shifts towards -3.1 . All these features are indicative of transitions in the dominant acceleration mechanisms and (or) the origin of the CRs and can be seen on Figure 1.1.

Below $\sim 10 \text{ GeV}$, the spectrum is significantly affected by solar modulation [33, 34], which prevents the lowest energy CRs from entering the inner Solar System. At higher energies, above the ankle, the cosmic-ray population is generally believed to become dominated by extragalactic sources [35, 36]. Moreover, the suppression of the CR population is believed to be due to the so-called Greisen–Zatsepin–Kuzmin (GZK) cutoff [37]. If this suppression truly reflects the GZK mechanism or the maximum energy achievable by cosmic accelerators remains an open question, strongly dependent on the, still uncertain, chemical composition of CRs at these energies.

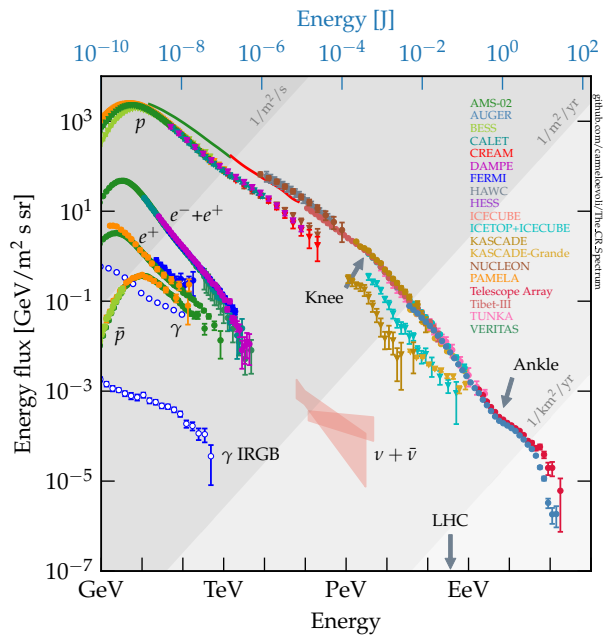


Figure 1.1: CR spectrum observed from at Earth [32].

Particularly relevant for the scope of this work is the feature known as the knee. This steepening of the spectrum has been interpreted as a signature of the maximum energy attainable by galactic accelerators. Supporting this interpretation is the observed gradual shift in chemical composition above a few PeV [38]. This compositional change suggests a nuclear charge dependant cutoff mechanism, so that the maximum energy reached in acceleration processes scales with the particle's electric charge. This way, the knee could be explained as the result of a superposition of individual cutoffs for each nuclear species.

To explore this possibility, one needs to understand what the galactic accelerators of CRs are and what properties they show. In particular, this framework requires that galactical sources produce CRs up to ~ 3 PeV, where the knee appears. While there are some well-established mechanisms that can, in principle, accelerate particles to PeV energies, reaching such energies requires extremely favorable conditions (namely, large acceleration regions and sufficiently high magnetic fields). Thus, the key open question is not whether a mechanism can account for PeV acceleration, but rather which astrophysical sources can provide an environment where the acceleration mechanism operates efficiently up to these energies.

To sum up the problem, regardless of the set of galactic accelerators considered, they should of course reproduce the observed luminosity of CRs in the galaxy. This is,

$$L_{\text{CR}} = \frac{U_{\text{CR}} V_{\text{MW}}}{\tau_{\text{conf}}} \approx 2.5 \cdot 10^{40} \text{ erg s}^{-1};$$

where $V_{\text{MW}} \approx 2 \cdot 10^{11} \text{ pc}^3$ is the volume of the Milky Way and $\tau_{\text{conf}} \approx 20 \text{ Myr}$ [39, 40] is the CR confinement timescale in the Galaxy.

At first, supernova remnants (SNR) where considered good PeVatron candidates, as the kinetic energy released in a supernova explosion is $E_{\text{SN}} \approx 10^{51} \text{ erg}$ [41] and the rate of supernova explosions occurring in the Milky Way is $\tau_{\text{SN}} \approx 0.02 \text{ yr}^{-1}$ [42]. In other words, the total power injected by supernova explosions is

$$L_{\text{SN}} = \frac{E_{\text{SN}}}{\tau_{\text{SN}}} \approx 6.3 \cdot 10^{41} \text{ erg s}^{-1},$$

which would be enough to account for the observed CR luminosity even if just a fraction of this power goes to accelerating CRs. However, one needs to understand the mechanism of acceleration to legitimate that such assumption is indeed correct.

This mechanism is called the *first-order Fermi mechanism* or the *Diffusive Shock Acceleration* (DSA) [43, 44]. The supersonic expansion of supernova explosion generates a collisionless shock wave that propagates through the interstellar medium (ISM). It is in this shocks that the DSA

takes place. To see how the process works in general words, let's consider the shock front as a discontinuity separating two regions with different plasma flow velocities: the upstream (unshocked plasma), moving at speed u_1 ; and the downstream (shocked plasma), moving at a slower speed $u_2 < u_1$ in the shock frame.

Charged particles entering the upstream region begin to diffuse due to magnetic turbulence, quickly becoming isotropic in velocity. Some of them cross the shock into the downstream region, where they diffuse again. Each time a particle crosses the shock back and forth, it effectively collides with plasma moving toward it, gaining energy in the process due to the velocity difference $|u_1 - u_2|$. This is a process analogous to that of a collision with a moving wall.

This repeated crossing and scattering leads to a systematic energy gain, as each shock cycle increases the particle's energy by an amount proportional to $\Delta E \propto (|u_1 - u_2|/c) \cdot E$. Over multiple cycles, particles can reach very high energies, making DSA a compelling mechanism for accelerating CRs in astrophysical shocks such as those produced by supernova remnants.

The maximum energy up to which supernova explosions can accelerate CRs by means of DSA can be estimated and results insufficient to arrive to the knee regime in the observed CR spectrum (at least in standard conditions) [45]. This then has led to continue the search of PeVatrons, where stellar clusters have recently gained importance. A brief discussion on this hypothesis is offered in the next section.

1.2 Introduction to stellar clusters physics

The question of what a stellar cluster is does not have a clear answer and is still under debate [46]. Different definitions have been used throughout time and are currently accepted, many of them establishing conditions regarding gravitational boundedness, mean mass density or minimal population [47, 48]. The implications of choosing one particular definition and the differences between them could be a topic of whole study and, in any case, is not of particular transcendence in the work that we will present here. Thus, we can simply define a stellar cluster as a group of stars that are gravitationally bound to one another.

Stellar clusters can also be classified regarding their morphology, total mass or age [46]; but far from entering in these kind of discussions, we will from now on focus on the so-called *young massive stellar clusters* (YMSCs). The reason behind these decision is that these are the good PeVatrons candidates: they are young enough to not having experienced a considerable amount of supernovae (not much older than 10 Myr) and sufficiently massive to produce significant CR

acceleration (with a total mass bigger than $10^3 M_{\odot}$).

It is important to note that the physics and evolution of stellar clusters can vary significantly depending on a multitude of factors, including their initial conditions, environment and stellar composition. However, in the case of the clusters relevant to this study, our interest does not lie primarily in the internal stellar dynamics or detailed stellar evolution, but rather in the collective effect of their stellar winds. These winds interact and combine to carve out a large-scale structure in the surrounding interstellar medium: a hot, low-density bubble bounded by a dense shell; which constitutes the environment where CR acceleration is thought to occur. This acceleration takes place mainly via the DSA mechanism previously mentioned.

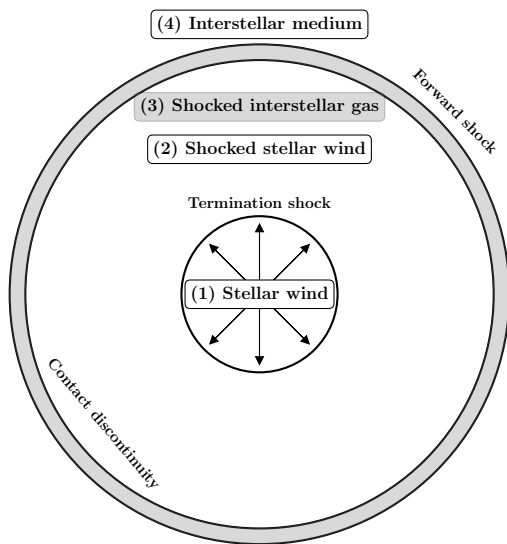


Figure 1.2: Stellar cluster wind bubble structure.

schematically shown in Figure 1.2. In this description, the stellar cluster is considered pointlike in the centre of the concentric spheres.

A useful theoretical framework to describe the evolution of such structures is provided by the classic model developed by Weaver in 1977 [49]. This model offers a simplified but physically insightful description of how continuous energy injection from stellar winds drives the formation and evolution of a wind-blown bubble in the surrounding interstellar medium. Despite its assumptions, such as spherical symmetry, a homogeneous ambient medium and a steady energy input, it captures the essential features of the system and provides analytical estimates for key quantities. In what follows, we briefly review the main aspects of this model relevant to our study.

To understand this environment, it is necessary to describe the basic structure of a stellar wind bubble. This system is typically divided into four concentric regions: (1) the freely expanding stellar wind, (2) the shocked stellar wind, (3) the shocked interstellar medium (ISM) and (4) the unperturbed ISM. These regions are separated by three key interfaces: the termination shock, where the supersonic stellar wind is decelerated and heated; the contact discontinuity, which separates wind material from swept-up ISM; and the forward shock, which compresses and heats the ISM as the bubble expands. This is

The model [49] divides the system's evolution into several stages, depending on the dominant physical processes at play. Each stage exhibits different scaling relations and structural features, making it essential to distinguish between them when modelling or interpreting observational data.

The early stage of bubble evolution, lasting typically $\sim 10^4$ yr, is characterised by an initial expansion driven by the cumulative effect of stellar winds. During this phase, the forward shock radius evolves as $R_{\text{FS}}(t) = AL_{\text{w}}^{1/5} \rho_0^{-1/5} t^{3/5}$, with A a dimensionless constant and L_{w} the wind luminosity. The cold wind termination shock and contact discontinuity positions, R_{TS} and R_{CD} , can also be approximated analytically under the assumption of an isobaric hot shocked wind region. However, due to the brevity of this stage and the breakdown of the adiabatic approximation as the cooling of the shocked ISM becomes important, it is not of practical relevance for our study. Therefore, in this work we focus on the subsequent *intermediate stage*, where the bubble has entered a self-similar expansion regime.

In this stage, the evolution of the bubble is mainly characterised by the start of radiative cooling being efficient in the hot shocked interstellar gas. As this radiative cooling is not included in the mathematical derivations, its effects are manually included by the assumption that the cooling causes an important contraction that leads to the shocked ISM to reduce its volume until it constitutes a thin shell around the shocked stellar wind. Thus, the approximation $R_{\text{CD}} \approx R_{\text{FS}}$ can be made, and we consider that the forward shock and the contact discontinuity are what define the *size* of the bubble. We therefore treat indifferently $R_{\text{B}} = R_{\text{CD}} \approx R_{\text{FS}}$. In this conditions, a force balance in the shell yields

$$\frac{d}{dt} \left[M_{\text{S}} \frac{dR_{\text{B}}}{dt} \right] = 4\pi R_{\text{B}}^2 P_{\text{SW}},$$

where M_{S} is the total mass contained in the shell and P_{SW} is the pressure in the region of shocked stellar wind.

This momentum balance can be put in terms of energy balance [49] where the wind luminosity, L_{w} , and the mean bubble density, ρ_0 , are used. After some easy calculations it is shown that

$$R_{\text{B}}(t) = \left(\frac{250}{308\pi} \right)^{1/5} L_{\text{w}}^{1/5} \rho_0^{-1/5} t^{3/5}. \quad (1.1)$$

An expression for the pressure P_{SW} can also be obtained, resulting in

$$P_{\text{SW}}(t) = \frac{7}{(3850\pi)^{2/5}} L_{\text{w}}^{2/5} \rho_0^{3/5} t^{4/5}.$$

However, what we are more interested about is that this expression can now be used to find the radius of the forward shock. Indeed, this discontinuity is characterised by the fact that it

is there where the ram pressure of the free expanding wind equates that of the shocked wind.

This is,

$$\frac{\dot{M}_w v_w}{4\pi R_{\text{TS}}^2(t)} = P_{\text{SW}}(t) = \frac{7}{(3850\pi)^{2/5}} L_w^{2/5} \rho_0^{3/5} t^{4/5},$$

from which we deduce

$$R_{\text{TS}}(t) = \sqrt{\frac{(3850\pi)^{2/5}}{28\pi}} \dot{M}_w^{1/2} v_w^{1/2} L_w^{-1/5} \rho_0^{-3/10} t^{2/5}. \quad (1.2)$$

The set of equations (1.1) and (1.2) describes the structural evolution of the bubble during the intermediate stage; when thermal conduction between the shocked wind and the ISM plays a key role and radiative cooling can be neglected in the bubble (but we still include the ad-hoc modification in the shocked ISM shell previously described). The seminal work by Weaver in 1977 [49] presents a much more detailed analysis, providing the full radial profiles of the relevant physical quantities. The physical discussions therein have shaped the understanding of stellar cluster bubbles over the past decades and provided the conceptual basis for subsequent improvements and extensions.

To derive these expressions, the work used one of the simplest forms of hydrodynamical motion equations,

$$\begin{cases} \frac{\partial \rho}{\partial t} + \mathbf{v} \cdot \nabla \rho + \rho \nabla \cdot \mathbf{v} = 0, \\ \frac{\partial \mathbf{v}}{\partial t} + \mathbf{v} \cdot \nabla \mathbf{v} + \frac{\nabla p}{\rho} = 0, \\ \frac{\partial p}{\partial t} + \mathbf{v} \cdot \nabla p + \rho c_s^2 \nabla \cdot \mathbf{v} = 0; \end{cases} \quad (1.3)$$

where, of course, only radial dependence was assumed. These equations describe mass, momentum and energy conservation in a compressible and non-viscous fluid. However, such formulation neglects various physical processes that can be of considerable importance in the structure and long-term evolution of stellar wind bubbles.

One of these is thermal conduction, which plays a key role in smoothing temperature gradients and regulating the transfer of energy between the hot shocked wind and the cooler surrounding material. Weaver considered this effect qualitatively by assuming that radiative cooling leads to a very thin shell structure, but a more rigorous approach includes an explicit conductive flux term in the energy equation. This term is typically modelled by the Fourier Law as

$$\mathbf{F}_{\text{class}}^{\text{cond}} = -\kappa(T) \nabla T, \quad (1.4)$$

where $\kappa(T)$ is the thermal conductivity, often taken to follow a Spitzer-type temperature dependence in astrophysical plasmas [50]. A more sophisticated expression can also be

considered to account for a saturation value, $F_{\text{sat}}^{\text{cond}}$, of the flux,

$$\mathbf{F}_{\text{cond}} = \left(\frac{F_{\text{sat}}^{\text{cond}}}{F_{\text{sat}}^{\text{cond}} + |\mathbf{F}_{\text{class}}^{\text{cond}}|} \right) \mathbf{F}_{\text{class}}^{\text{cond}}. \quad (1.5)$$

The divergence of this flux then acts as a source term in the energy equation, accounting for the redistribution of thermal energy within the bubble.

Another relevant physical process is optically thin radiative cooling, particularly important in dense regions of the shell or at late evolutionary stages of the bubble. Radiative losses can be included via a cooling function $\Lambda(T)$, leading to an energy sink term in the energy equation of (1.3). There are many ways of choosing the cooling function, but one approach is to use a simple power law,

$$\Lambda_{\text{pl}}(T) \propto \rho^2 T^\alpha. \quad (1.6)$$

This type of temperature dependence arises, for example, when bremsstrahlung is the dominant emission mechanism.

While the Weaver model captures the essential physics and yields qualitatively accurate descriptions, it falls short in reproducing certain quantitative aspects: most notably the observed bubble sizes, which tend to be considerably smaller than predicted. One major limitation lies in the assumption of spherical symmetry. Observations clearly indicate that hydrodynamic and magnetohydrodynamic instabilities arise early during the expansion, quickly distorting the bubble's shape and increasing the surface area of the interfaces [51, 52]. This enhances conductive energy losses, which in turn reduces the expansion rate. Furthermore, accounting for radiative cooling throughout the entire evolution and not just in later stages is also expected to reduce the predicted size of the bubble.

Although many recent works have moved towards multidimensional approaches in order to capture hydrodynamical instabilities and abandon spherical symmetry, there is, to our knowledge, no one-dimensional model that both retains computational simplicity and yields more accurate predictions than the Weaver solution. This project aims to provide such a model, in order to develop a public computational tool that can serve as a practical and accessible resource for the community.

1.3 The transport equation

To the moment, we have presented the problem regarding CRs origin and why stellar clusters are relevant in the subject. A brief introductory text in regard to stellar cluster bubbles has also been provided. However, we still need a mathematical and physical foundation for how the

analysis of CR acceleration is going to be made. This is why we now introduce the transport equation.

As previously discussed, CR acceleration in stellar clusters is believed to occur primarily via the DSA mechanism at the termination shock of the collective stellar wind. While a direct numerical modelling of DSA would provide a more complete description, it lies beyond the scope of this work, as it would require a much more complex treatment. Instead, we adopt a simplified approach: we consider that the termination shock acts as an effective source of already accelerated CRs, injecting a predetermined distribution function into the system. The focus of our analysis is therefore not on the acceleration process itself, but on the subsequent propagation and evolution of these CRs throughout the interior of the bubble.

Understanding how the injected particles are transported under the combined influence of advection, diffusion and energy losses is essential for predicting the resulting observable signatures. In particular, solving the transport equation allows us to estimate the spectro-morphological distribution of the CR population at different times. From this and the interaction with radiation and magnetic fields in the region, one could in principle compute the expected non-thermal emission, such as the γ -ray spectrum produced through hadronic interactions or inverse Compton scattering. However, the derivation of the resulting observable spectrum lies beyond the scope of this thesis and would constitute a dedicated project on its own. The goal of the present work is to lay the necessary foundation by developing a consistent framework that couples the simulation of the stellar wind bubble with the evolution of the CR distribution within it. These results can then be used as the starting point for future studies focused on the prediction of emission spectra and their comparison with observations.

In this context, the transport equation that is relevant to our study is

$$\frac{\partial f}{\partial t} + \nabla \cdot (\mathbf{u}f) - \frac{\partial}{\partial p} \left(\frac{p}{3} (\nabla \cdot \mathbf{u}) f \right) = \nabla [D \nabla f] + Q;$$

where $f(t, \mathbf{r}, \mathbf{p})$ is the distribution function of the CRs, $D(t, \mathbf{r}, \mathbf{p})$ is the diffusion coefficient and $Q(t, \mathbf{r}, \mathbf{p})$ is a source term. Here, \mathbf{u} is the velocity field within which CRs are advected, this is to say, the velocity of the bubble wind. Assuming spherical symmetry and only radial dependence, this equation can be rewritten as

$$\frac{\partial f}{\partial t} + \frac{1}{r^2} \frac{\partial(r^2 u_r f)}{\partial r} - \frac{\partial}{\partial p} \left[\frac{p}{3} \left(\frac{1}{r^2} \frac{\partial(r^2 u_r)}{\partial r} \right) f \right] = \frac{1}{r^2} \frac{\partial}{\partial r} \left(r^2 D \frac{\partial f}{\partial r} \right) + Q.$$

In order to have a complete problem, this equation needs to be solved with particular

boundary and initial conditions. In our specific case, the boundary conditions¹ are

$$\frac{\partial f}{\partial r}(t, 0, p) = 0 \quad \text{and} \quad f(t, R_{\text{end}}, p) = f_{\text{ISM}}(p).$$

While the initial condition yields

$$f(0, r, p) = f_{\text{DSA}}(p)\delta(r - R_{\text{TS}}).$$

To sum up, the problem of transport that we will aim to solve numerically is

$$\begin{cases} \frac{\partial f}{\partial t} = -\frac{1}{r^2} \frac{\partial(r^2 u_r f)}{\partial r} + \frac{\partial}{\partial p} \left[\frac{p}{3} \left(\frac{1}{r^2} \frac{\partial(r^2 u_r)}{\partial r} \right) f \right] + \frac{1}{r^2} \frac{\partial}{\partial r} \left(r^2 D \frac{\partial f}{\partial r} \right) + Q, & r \in (0, R_{\text{end}}), \quad p \in \mathbb{R}^+, \quad t \in \mathbb{R}^+; \\ \frac{\partial f}{\partial r}(t, 0, p) = 0, \quad f(t, R_{\text{end}}, p) = f_{\text{ISM}}(p), & p \in \mathbb{R}^+, \quad t \in \mathbb{R}^+; \\ f(0, r, p) = f_{\text{DSA}}(p)\delta(r - R_{\text{TS}}), & r \in (0, R_{\text{end}}), \quad p \in \mathbb{R}^+. \end{cases} \quad (1.7)$$

To the best of our knowledge, no existing public numerical code currently implements a solver for the CR transport equation in spherical symmetry. In particular, the simultaneous inclusion of advection, diffusion, energy losses and source injection within a dynamically evolving wind bubble structure is not addressed by standard tools. For this reason, as part of the present work, we have developed a complete and dedicated numerical routine specifically designed to solve the above system. This solver constitutes one of the main methodological contributions of the thesis and provides a flexible framework for future studies aiming to couple stellar cluster environments with CR propagation and emission modelling.

¹The physical condition is that $\lim_{r \rightarrow \infty} f(t, r, p) = f_{\text{ISM}}(p)$, but numerically we can simplify the implementation by assuming $R_{\text{end}} \gg R_{\text{B}}$.

Chapter 2

Simulating stellar clusters with PLUTO

2.1 What is PLUTO?

PLUTO is a high-performance, modular and highly versatile numerical code designed to solve systems of conservation laws relevant to fluid dynamics in astrophysical contexts. Originally developed by A. Mignone and collaborators [53], it has become a widely used tool in computational astrophysics due to its flexibility, accuracy and ability to model a wide range of physical processes across different regimes.

At its core, PLUTO integrates a general system of partial differential equations in conservation form, expressed as

$$\frac{\partial \mathbf{U}}{\partial t} + \nabla \cdot \mathbf{T}_h(\mathbf{U}) = \nabla \cdot \mathbf{T}_p(\mathbf{U}) + \mathbf{S}(\mathbf{U}),$$

where \mathbf{U} denotes the set of conservative variables, \mathbf{T}_h the hyperbolic (advective) flux tensor, \mathbf{T}_p the parabolic (diffusive) flux tensor and $\mathbf{S}(\mathbf{U})$ the source terms. The system is typically closed with an equation of state and variables are converted between conservative and primitive forms as needed.

PLUTO supports a wide array of physical modules, enabling simulations of magnetohydrodynamical flows in different regimes even including relativistic approaches. However, it is the classical hydrodynamics model that we will make use of in this work. These different modules can be enabled independently, allowing the user to tailor the solver to the specific physical processes of interest. Non-ideal effects such as viscosity, thermal conduction or optically thin radiative cooling are also available via additional modules.

A key strength of PLUTO lies in its use of finite volume method (FVM) and finite difference shock-capturing schemes. These are designed to handle highly non-linear flows with strong discontinuities such as shocks and contact surfaces, which is exactly what the systems that we will study exhibit. The FVM relies on a conservative formulation that tracks the evolution of cell-averaged quantities over time. In this framework, the computational domain is discretised into control volumes and the time evolution of the solution depends critically on the accurate evaluation of fluxes across the interfaces between adjacent cells. This is where the so-called Riemann solvers come into play.

In the context of FVM, a Riemann problem is a local initial value problem consisting of a single discontinuity between two constant states. At each cell interface, this discontinuity approximates the local solution structure and the Riemann solver provides a numerical flux based on the evolution of this discontinuity. Therefore, the design and choice of Riemann solvers is a central aspect of FVM schemes, as it determines the method’s ability to accurately capture shocks, rarefactions and contact discontinuities in the flow. In this sense, PLUTO implements a variety of Riemann solvers and time integration schemes that the user can choose depending on their needs.

PLUTO also supports multiple geometries and, in particular, it allows simulations in spherical coordinates with one-dimensional symmetry. This feature is especially relevant for our study. Although the computational grid can be dynamically refined using adaptive mesh refinement, such an approach would introduce considerable complexity into the subsequent systematic analysis, exceeding the scope of this project. For this reason, a static grid has been employed.

The code is fully parallelizable using MPI and is well suited for high-performance computing on modern computational clusters. In fact, although we initially performed serial simulations, we soon transitioned to parallel runs, observing a notable improvement in performance.

Its modular design also allows for easy integration of user-defined routines to account for additional physics and to set initial and boundary conditions, making it a flexible platform for custom setups.

Related to this is another important reason for choosing PLUTO: its open-source nature. As an open-science tool, it allows full access to the source code, ensuring transparency, reproducibility and the possibility of modification or extension by the user. This is particularly advantageous in a research context, where adapting existing tools to new problems is often necessary.

Moreover, PLUTO is written in the C programming language and is designed to be compiled and executed via the command-line interface. This facilitates the integration of simulations within automated workflows through Bash and Python scripting. Such automation enables large parameter sweeps, batch processing and the development of additional tools for data pre- and post-processing, analysis or visualization. For this project, custom scripts were developed to compile and run simulations, manage outputs and systematically explore the dependence of the results on various physical parameters.

In this work, PLUTO has been employed to perform hydrodynamic simulations of wind-blown bubbles in young stellar clusters. In the next sections, we show how these simulations provide the structural background in which cosmic ray transport is subsequently modelled, making PLUTO a critical component of the multi-stage framework developed in this thesis.

2.2 Configurations considered

The motivation behind conducting these simulations is clear: obtaining the spatial and temporal evolution of the bubble profiles is essential for a subsequent cosmic ray propagation within them. Simpler approaches could certainly have been considered. For instance, one might rely directly on the analytical solution provided by the Weaver model and perform cosmic ray simulations on top of it. This would, in principle, allow for simpler numerical implementations and greater computational efficiency. However, such an approach would not significantly advance the current state of the art and the expected results would presumably be comparable to those already available in the literature. For this reason, we chose to perform our own simulations, so that to gradually increase the physical complexity of the model until sufficiently refined results were obtained.

The initial conditions of all the simulations that we will present here are well known in the literature [54] for leading to inflated bubble structures as the one presented in Figure 1.2. In brief, the system initially consists of a sphere of 100 pc divided in three sections: a cluster core of radius ~ 0.1 pc, a sphere of wind injection of ~ 1 pc and the rest of the domain, which correspond to the surrounding ISM. These values may slightly vary in some configurations because: the grid considered might not lay in the exact points to achieve these radius and some simulations are based on real cluster parameters, which require some slight modifications of the prescribed magnitudes. In any case, the behaviour of the system is never modified by these variations.

Regarding the three initial regions mentioned, the cluster core is a region with fixed constant parameters, which is not evolved in the simulation. It serves as to account for the volume of the

cluster and to provide boundary conditions. The wind injection region is set initially following the analytical results of Weaver [49], this is, it is a region with constant wind velocity, v_w , and thus a density profile that decreases as $\rho(r) \propto r^{-2}$ because of mass conservation. Pressure in this intermediate region is set as to account for the temperature and the ram pressure of the wind. The temperature of the wind, T_w , is known to be unimportant regarding the system dynamics, and this irrelevance has been tested with our simulation. Thus, no important assumptions are done in the selection of T_w . Regarding the surrounding ISM, which initially constitutes the majority of the domain, the values chosen are the ones used in the literature [54]. At $r = 100$ pc, outflow boundary conditions are always imposed (although the dynamics of the system never reach the domain bounds).

Regarding the discretization of the domain, the number of points in the radial direction has been decided to be between 1000 and 3000, depending on the complexity of the structures appearing and the computational workload. In every situation, the spatial discretization is enough to fully resolve and have the solutions converged, so no further discussion about this aspect needs to be done. This is, indeed, one of the strengths of having stuck to one dimensional models, as the only coordinate being calculated in our simulations is the radial, with azimuthal and polar directions being irrelevant due to symmetry assumptions. Detailed information on how this is treated from a numerical point of view can be found in [53].

With respect to the choice of Riemann solver, we initially made use of a Lax-Friedrichs scheme due to its simplicity and robustness. This solver provides a very diffusive but stable solution and was a good starting point for testing general code behaviour. However, its high numerical diffusion tends to smooth out discontinuities, such as shocks or contact interfaces, which resulted inconvenient for our study.

To improve accuracy, especially in capturing the structure of the wind bubble and its associated discontinuities, we later adopted a more sophisticated Harten-Lax-van Leer (HLL) approximate solver. In particular, we made use of the HLLC implementation provided by PLUTO, which provides specific routines to restore the middle contact discontinuity absent in the simpler HLL scheme. This is particularly important in our context, where the correct resolution of contact surfaces such as the interface between shocked wind and shocked ISM is critical. The HLLC solver proved to yield more accurate and physically consistent results in our simulations and was therefore chosen as the default solver in the final runs.

For completeness, it is convenient to mention here some other technical numerical details. As is common in the numerical simulation of continuous physical systems and we already discussed,

the solution is discretised and computed at a set of nodes defined over a spatial grid. However, in order to evaluate fluxes at cell interfaces and to extract smooth profiles from discrete data, interpolation between these nodes is required both during and after the simulation runtime. How such interpolation is done is defined the *reconstruction* method.

Reconstruction techniques can vary in complexity, ranging from simple polynomial fits to more sophisticated schemes that employ weighted nodes and special functional bases to avoid non-physical oscillations. In all the simulations presented in this work, a piecewise linear reconstruction is applied to the primitive variables, the implementation that PLUTO provides is supplemented by a Total Variation Diminishing (TVD) limiter to control spurious oscillations near sharp gradients or discontinuities. This method achieves second-order accuracy in space and relies on a three-point stencil (that is, it uses each cell and its two immediate neighbours to estimate the solution gradient across interfaces).

In regard to time discretization, a second-order TVD Runge-Kutta scheme is used. The time step determination is managed by PLUTO using the information of previous integration steps and imposing a CFL condition that can be slightly adjusted by the user in order to fulfil stability criteria. Detailed information about the specific temporal treatment done by PLUTO for every combination of selected modules and solvers can be found in [53].

We now turn our attention to the specific numerical simulations carried out in this work, focusing on their parameter choices and implementation details. All of the simulations that we will present in the next section, unless otherwise stated, are carried out under the consideration of a fiducial stellar cluster model, whose properties are chosen to be representative of typical YMSCs. In particular, we will consider¹ $\dot{M} = 10^{-4} \text{ M}_{\odot} \text{ yr}^{-1}$ and $L_w = 10^{38} \text{ erg s}^{-1}$. The chemical composition of the system is assumed to be purely neutral particles with proton masses.

With this setup, the system of equations presented in (1.3) is computed, always complemented with an ideal equation of state,

$$p = nk_{\text{B}}T = \frac{\rho}{m_u\mu}k_{\text{B}}T;$$

where n the particle number density, k_{B} the Boltzmann constant, m_u the atomic mass unit and μ the mean molecular weight. In our case of fully protonic gas, $\mu = 1$.

In the first simulation presented, we study this simple model in order to observe the basic dynamics of the system and the formation of wind-blown bubbles under idealised conditions. This configuration serves as a benchmark to verify the implementation, test the numerical

¹Note that v_w is determined by the relation $L_w = \frac{1}{2}\dot{M}v_w^2$.

stability of the setup and identify the qualitative behaviour of the main flow features. However, we soon move towards more complex and physically realistic scenarios by progressively incorporating additional physical processes that play a significant role in the evolution of stellar cluster bubbles.

To study thermal conduction, we consider several simulations with varying assumptions. Notably, the default value conductivity implemented in PLUTO, $\kappa_{\text{PLUTO}}(T)$, differs from the classical Spitzer formulation typically used in astrophysical plasmas [50]. We therefore perform simulations using both the PLUTO default value and the standard Spitzer conductivity, allowing us to quantify the impact of this choice on the bubble structure. Furthermore, we explore the effects of conduction saturation: by comparing simulations with and without saturation effects, we evaluate their influence on the evolution of the system.

In parallel, we investigate the influence of optically thin radiative cooling. To this end, we conduct a set of simulations with varying intensities of the cooling function, effectively modifying the strength of radiative losses. This allows us to understand the degree to which cooling shapes the dynamics of the bubble, particularly in the dense outer shell. Additionally, we examine the numerical consequences of enabling the `SHOCK_FLATTENING` routine provided by PLUTO, which is designed to enhance stability near strong shocks and prevent non-physical oscillations in the presence of steep gradients.

Finally, we bring together all the relevant physical processes (thermal conduction and radiative cooling) in a simulation tailored to a real astrophysical object: the young massive cluster M16, *the Eagle Nebula*. This final case aims to provide a more realistic representation of stellar feedback in a galactic environment and serves as a proof of concept for the applicability of our approach to observationally motivated scenarios.

2.3 Results

2.3.1 Purely hydrodynamical system

The results for the radial profiles of density, wind velocity, pressure and temperature in the case of a purely hydrodynamical system are shown in Figure 2.1, where we present the evolution of the system under the parameters and initial conditions reported in Section 2.2 after a time of $t = 7$ Myr.

The density subplot reveals four distinct regions, which correspond precisely to those described schematically in Figure 1.2. Starting from the centre of the sphere, where the stellar

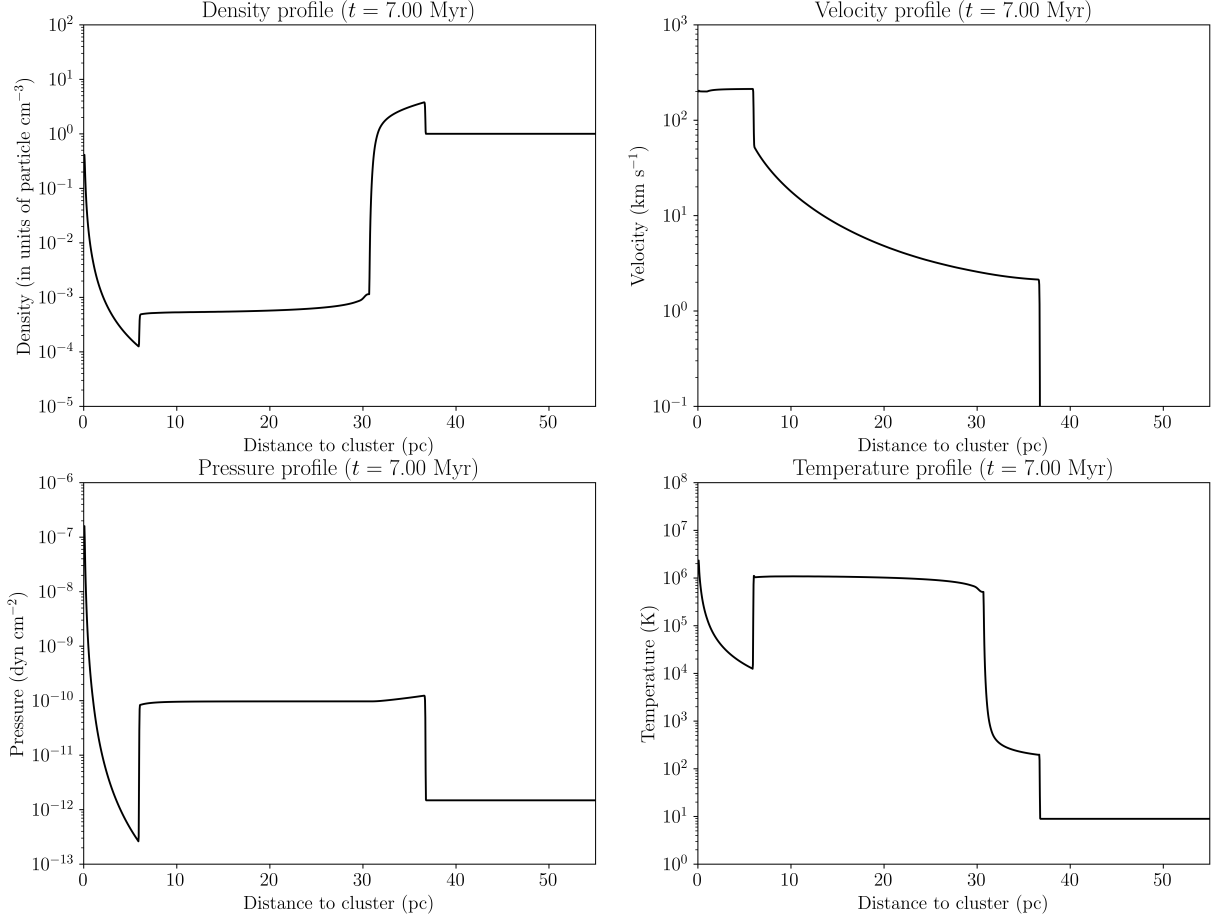


Figure 2.1: Results for the radial profiles of density (upper left panel), velocity (upper right panel), pressure (lower left panel) and temperature (lower right panel), obtained for a bubble using a purely hydrodynamical model. Initial conditions and parameters are detailed in Section 2.2.

cluster is located, the first region is characterized by a density profile that decreases as $\rho \propto r^{-2}$. This behaviour is due to from mass conservation and can be derived in a spherically symmetric outflow assuming that the wind velocity remains approximately constant. This assumption is validated by the simulation results, as the velocity plot confirms that the wind speed is indeed roughly uniform throughout this region.

After the first 7 Myr, the simulation shows the termination shock located at approximately ~ 6 pc from the cluster center. This shock is marked by a discontinuity in all physical quantities and shows the beginning of the shocked wind. Just behind it, the density profile flattens, defining the *bubble*; that is, the volume filled with shocked stellar wind material. One notable feature is that this entire region remains approximately isobaric and isothermal (as we assumed an ideal

equation of state). These conditions are often postulated in analytical models and our numerical results provide support for their validity.

At around ~ 32 pc, a sharp contact discontinuity becomes evident in the density profile, indicated by a significant jump. This discontinuity separates the shocked wind from the shocked interstellar medium. A key characteristic of contact discontinuities is that, unlike shocks, they do not involve jumps in either pressure or velocity. In our results, both quantities remain continuous across this interface, as expected. This behaviour confirms the nature of the discontinuity and supports the theoretical prediction that the pressure in the shocked wind and the shocked ISM must be equal at the contact surface.

Beyond the contact discontinuity, the shell of shocked ISM exhibits a finite and clearly visible thickness, which seems contradictory to the approximation used in the Weaver model, where $R_{\text{CD}} \approx R_{\text{FS}}$. This discrepancy is expected, as the assumption in the analytical model is introduced *ad hoc* to account for physical effects not explicitly described by the mathematical formulation.

Finally, the forward shock, located at approximately ~ 36 pc, outlines the transition to the unperturbed interstellar medium. Indeed, this region consists of cold, steady ambient gas².

Given these results, it is natural to compare them with the time evolution predicted by the Weaver model. Although exact quantitative agreement is not expected (since, as previously discussed, some of Weaver’s assumptions are not strictly satisfied in our setup), we do expect qualitatively similar trends. In particular, by tracking the position of maximum density over time, one can estimate the evolution of the bubble radius, which in the Weaver framework follows the analytical expression given by (1.1). Such comparison is shown in Figure 2.2.

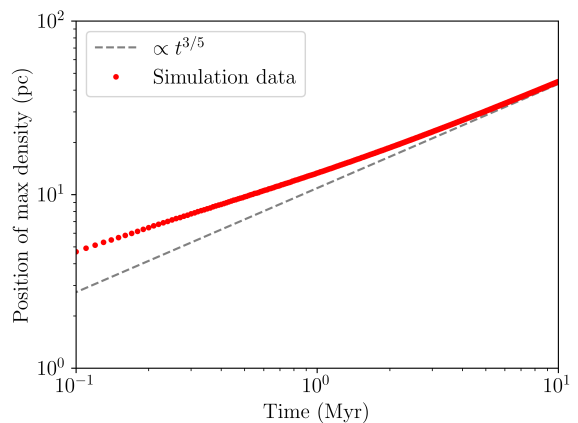


Figure 2.2: Position of maximum density over time for the hydrodynamic simulation corresponding to Figure 2.1. Comparison with the $\propto t^{3/5}$ predicted by Weaver’s model [49].

The figure illustrates that the simulation does not exactly reproduce the power-law scaling derived by Weaver [49]. However, the overall trend remains close, and the deviation observed is within acceptable bounds, especially

²Which is imposed by initial conditions

considering the simplifying assumptions made in the analytical model.

2.3.2 Thermal conduction

Let us now analyse the results regarding the simulations in which the additional conductive term, given by the expression (1.5), is included in the computation. As we mentioned in previous discussions, the treatment of thermal conduction can be done whether by taking into account saturation effects or by neglecting them. Moreover, the typical value of conductivity used in astrophysical plasmas is given by Spitzer [50] as

$$\kappa_S(T) \approx 1.2 \cdot 10^{14} \left(\frac{T}{10^8 \text{ K}} \right)^{5/2} \text{ erg s}^{-1} \text{ K}^{-1} \text{ cm}^{-1}.$$

However, PLUTO offers a default value for conductivity which reads

$$\kappa_{\text{PLUTO}}(T) \approx 5.6 \cdot 10^{13} \left(\frac{T}{10^8 \text{ K}} \right)^{5/2} \text{ erg s}^{-1} \text{ K}^{-1} \text{ cm}^{-1}.$$

This is to say, $\kappa_S \approx 2\kappa_{\text{PLUTO}}$. In order to investigate the relevance of the particular choice between both conductivities, we perform a set of simulations using both parameters (κ_S and κ_{PLUTO}) each tested with and without saturation effects. This allows us to evaluate the sensitivity of the system's evolution to the specific choice of thermal conductivity and to the inclusion of saturation. The results of this analysis is shown in Figure 2.3.

Figure 2.3 shows the state of the system at $t = 4$ Myr for the different conduction configurations. All configurations are compared against the fiducial purely hydrodynamical case. It is evident that none of the simulations exhibit significant deviations from the hydrodynamical reference. Only the case with saturated conduction shows a slight difference in the internal structure of the bubble, while the simulation without saturation remains nearly indistinguishable from the fiducial case.

Although the question of whether or not to include saturation will be addressed in more detail in the following discussion, it is already clear from Figure 2.3 that the specific choice of thermal conductivity (this is to say, whether using κ_S or κ_{PLUTO}) has negligible impact on the global evolution of the system. For this reason, we adopt the Spitzer conductivity κ_S as our standard choice in the remaining simulations.

Let us now turn our attention to the analysis of saturation effects. As it is not clear from Figure 2.3 how important for the dynamics of the system it is to include or not a saturation approach, we present a new set of simulations specifically designed to clarify this point.

In order to do the analysis, we will perform simulations in the same conditions than those presented in the Figure 2.3. We will have two groups of simulations: one group in which

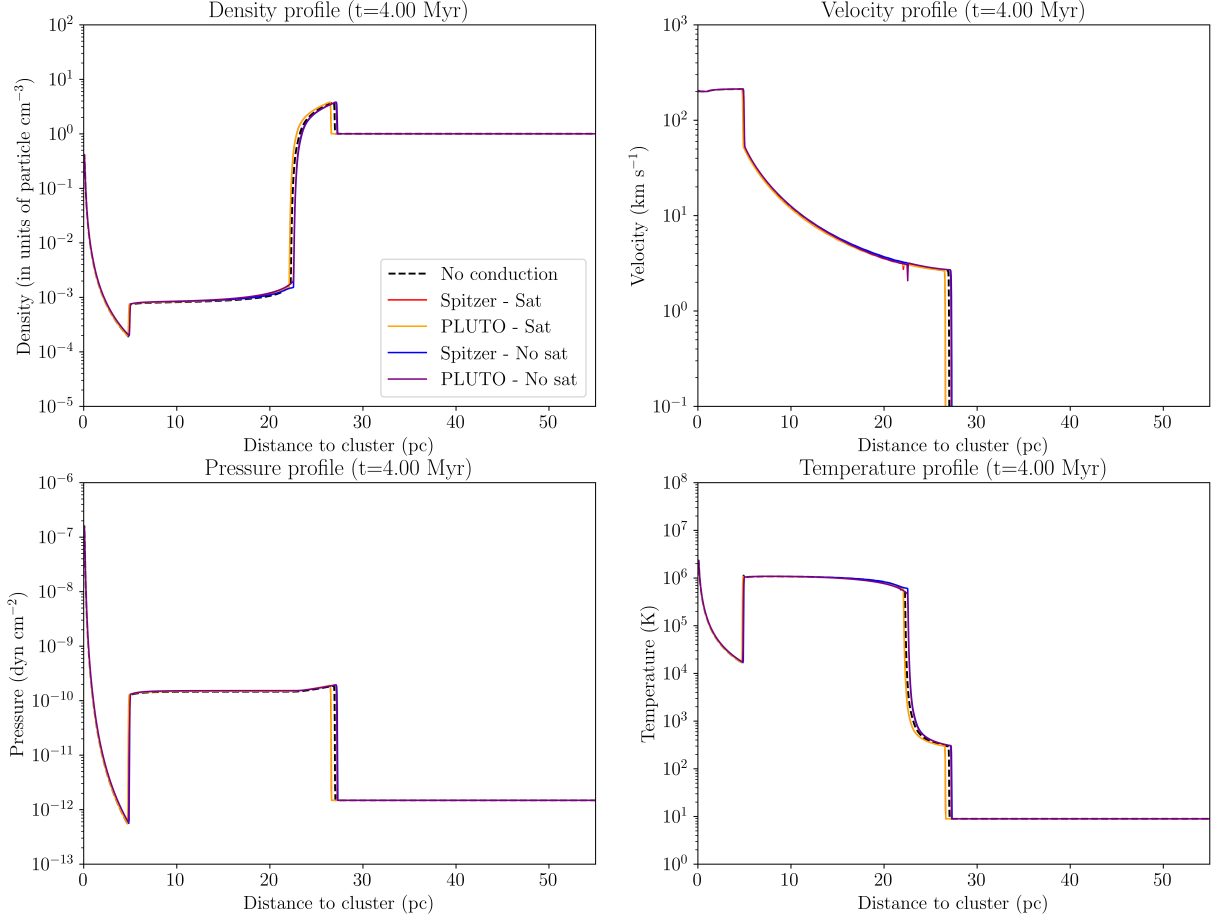


Figure 2.3: Comparison between the results for a purely hydrodynamical model and the different possible implementations for conduction. No important deviations are observed, so the election of conductivity results unimportant. Initial conditions and parameters are detailed in Section 2.2.

saturation effects will be taken into account and another one in which the classical conductive flux without saturation will be the one used.

For both groups of simulations, we have progressively increased the value of conductivity, multiplying by different scalars, in order to better understand the influence that the different conduction schemes have in the system. The results corresponding to the simulations with saturation are presented in the Figure 2.4 and those without saturation are shown in the Figure 2.5.

Figure 2.4 shows the results of the simulations where saturation effects are included in the conductive flux. A key observation is that we have been able to increase the conductivity up to 1000κ without encountering major numerical instabilities. As expected, increasing the thermal

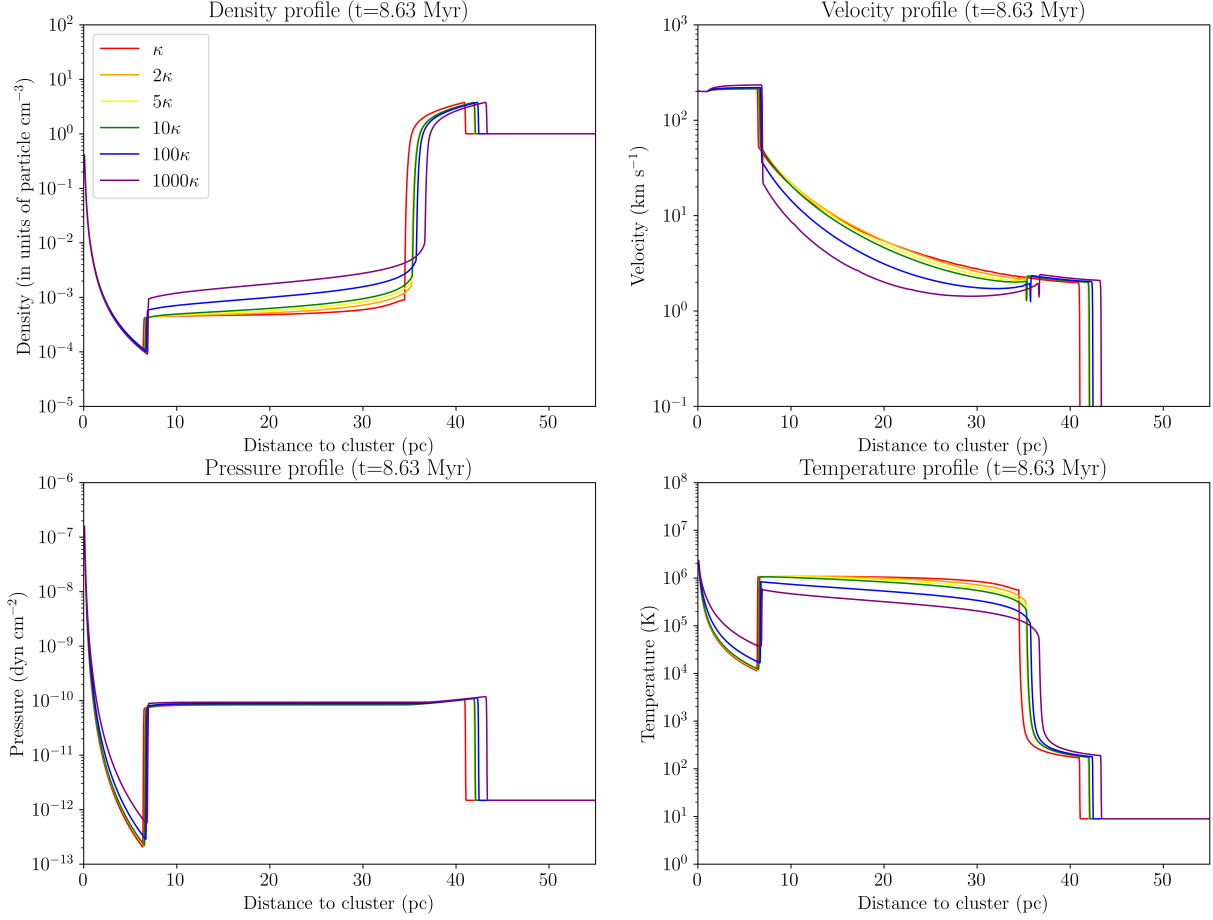


Figure 2.4: Results for the radial profiles obtained by increasing conductivities and using a model implementing saturation in the computation of conduction. Initial conditions and parameters are detailed in Section 2.2. We have used Spitzer’s conductivity [50].

conductivity significantly influences the structure of the bubble. At a fixed time ($t = 8.63$ Myr), we observe clear shifts in the positions of the termination shock, contact discontinuity and forward shock. These displacements are consistent with the interpretation of enhanced energy transfer from the hot interior to the outer regions. Moreover, the density within the shocked wind region increases with conductivity, as stronger conduction may promotes mass exchange from the dense, cooler shell into the hotter, less dense bubble interior. However, it is worth noting that the decrease in shell density is not visually evident in the plot due to the logarithmic scale. The density gain inside the bubble (of the order of 10^{-3} cm^{-3}) is relatively small compared to the typical ISM density of $\sim 1 \text{ cm}^{-3}$, and thus does not produce an appreciable change in the dense shell, which remains around $\sim 4 \text{ cm}^{-3}$. Future works on simulating this specific setup

might provide further proof for our interpretations.

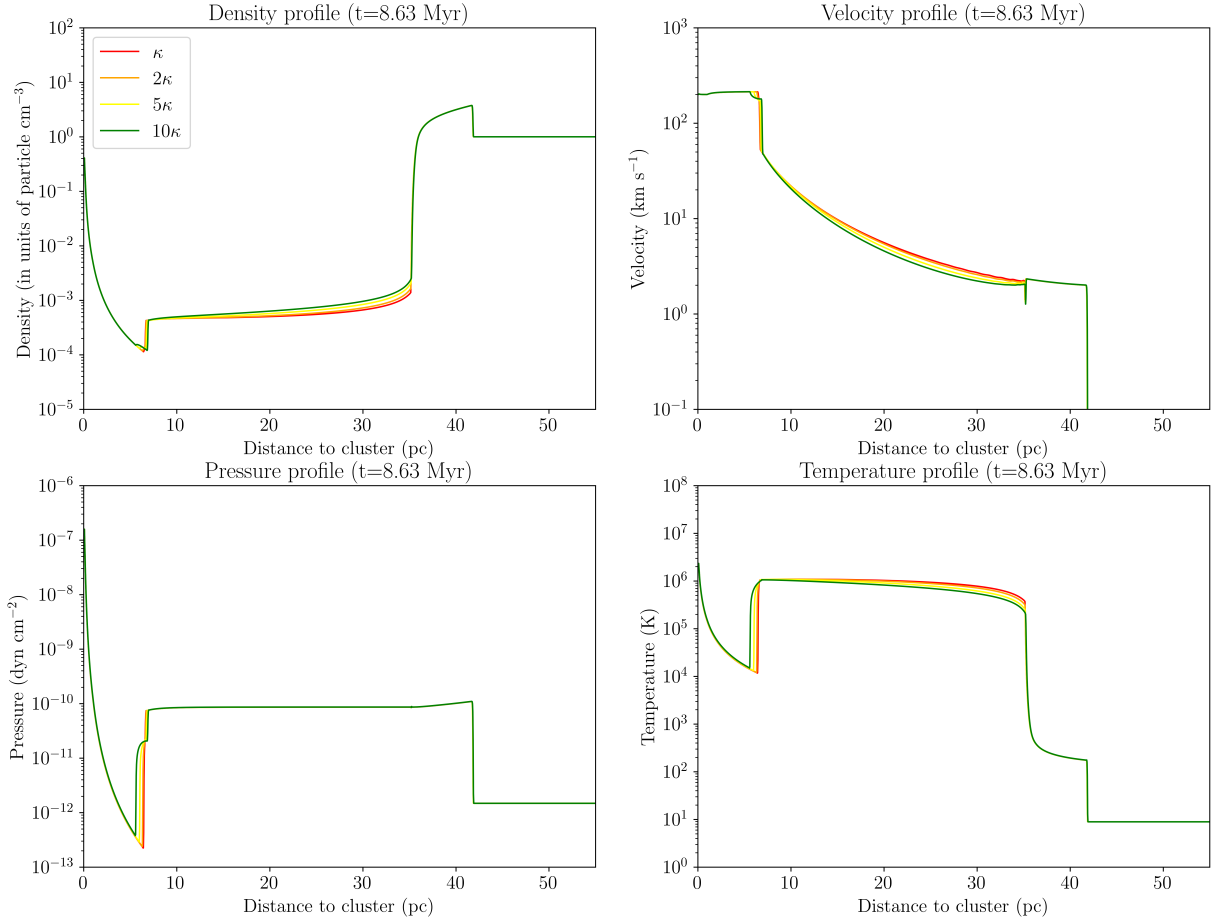


Figure 2.5: Results for the radial profiles obtained by increasing conductivities and using a model implementing no saturation in the computation of conduction. Initial conditions and parameters are detailed in Section 2.2. We have used Spitzer’s conductivity [50].

In contrast, Figure 2.5 presents the results for simulations in which saturation effects are not included. In this case, the behaviour is qualitatively different and notably less physical. First, the profiles show only very subtle changes as the conductivity is increased, especially regarding the positions of the shocks and contact discontinuity, which remain virtually unchanged across all tested values. Furthermore, we encountered severe numerical instabilities when trying to increase conductivity beyond 10κ , which prevented the code from completing the simulations. Even within this limited range, some numerical artifacts are visible, particularly near the termination shock, where non-physical fluctuations suggest a breakdown of the solution. These results reinforce the importance of including saturation effects when

modelling conduction in hot, rarefied astrophysical plasmas, as neglecting them not only leads to unrealistic dynamics but also compromises the numerical stability of the simulations.

2.3.3 Radiative cooling

After having understood the limitations of the implementation of conductivity and what the optimal configuration for our setups is, we repeat the same study with radiative cooling. To this end, the conductive term is removed so as to study only the impact of radiative cooling.

As we mentioned in previous sections, the mathematical formulation of radiative cooling is by means of a source term in the energy equation of the system (1.3). The simplest possibility which is supported by physical arguments is to construct the cooling function by means of a power-law, like we demonstrated in the expression (1.6), however, several alternatives are also possible. Many more complex analytical expressions exist that try to model detailed atomic and plasma processes across a wide range of temperatures and compositions. Nonetheless, such expressions typically involve increased computational cost and model complexity, which is what we want to avoid.

From a numerical perspective, an alternative to implementing complex analytic forms is to tabulate the cooling function over a relevant temperature range. In this approach, the function is precomputed and stored as a table, and during runtime the appropriate value is obtained via interpolation. PLUTO provides a default cooling table of this kind, constructed for an optically thin plasma with solar abundances. One question, therefore, is which of these approaches (power-law or tabulated) offers the best balance between physical fidelity and numerical efficiency for our specific problem.

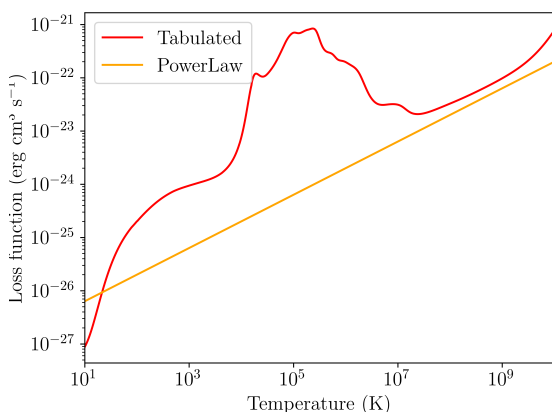


Figure 2.6: Comparison of loss functions implemented in PLUTO by the tabulated method or the default power-law with $\alpha = \frac{1}{2}$.

To evaluate difference between these cooling schemes, we conducted an analysis similar to the one previously carried out for thermal conductivity. Specifically, we compared the results obtained using the power-law cooling function with those obtained using the tabulated function provided by PLUTO. The outcomes showed only minor differences in the evolution and structure of the system, with no significant qualitative deviations. Due to the limited

relevance of these results and space constraints, we do not include detailed plots in this manuscript. However, given its greater physical realism and ease of use, we adopt the tabulated approach as the standard cooling method for the remainder of this work.

To better understand the differences between both models, Figure 2.6 displays the temperature dependence of the two cooling functions: the power-law with exponent $\alpha = \frac{1}{2}$ and the tabulated loss function used internally by PLUTO. As can be seen, the tabulated cooling function exhibits higher cooling rates over most of the temperature range, which is expected given its derivation from detailed atomic physics for an optically thin plasma with solar abundances.

What is of more interest is the influence of radiative cooling on the dynamics of the system. To investigate it, we perform a new set of simulations in which the intensity of the cooling function is progressively reduced. This is done by applying scaling factors to the values in the tabulated loss function provided by PLUTO, so as to diminish the overall strength of radiative losses.

The initial set of simulations performed with progressively reduced cooling intensities produced results that were numerically unstable and physically inconsistent. In particular, unphysical oscillations appeared near strong shocks, which is a classical sign of numerical instability and lack of convergence. To address this issue, we activated the `SHOCK_FLATTENING` subroutine provided by PLUTO, which is specifically designed to improve the robustness of the numerical scheme in regions with steep gradients. This routine acts by locally increasing numerical dissipation around strong shocks, suppressing spurious artifacts. Once activated, the simulations produced smooth and physically meaningful profiles, restoring the expected behaviour of the system. As a result, this option is enabled in all subsequent simulations presented in this work.

All these results are presented in Figure 2.7. The Figure shows the radial profiles of density, velocity, pressure and temperature for the set of simulations with progressively reduced radiative cooling. One of the most striking outcomes can be seen in the velocity plot (top right), where strong numerical instabilities manifest as large, non-physical oscillations over almost the whole domain.

In contrast, the simulation in which the `SHOCK_FLATTENING` subroutine was activated was performed using the same radiative cooling table as the `Tab` case but results in a much more stable and physically consistent solution. Notably, the discontinuities are cleanly resolved and the velocity profile no longer exhibits artificial noise, highlighting the importance of this numerical

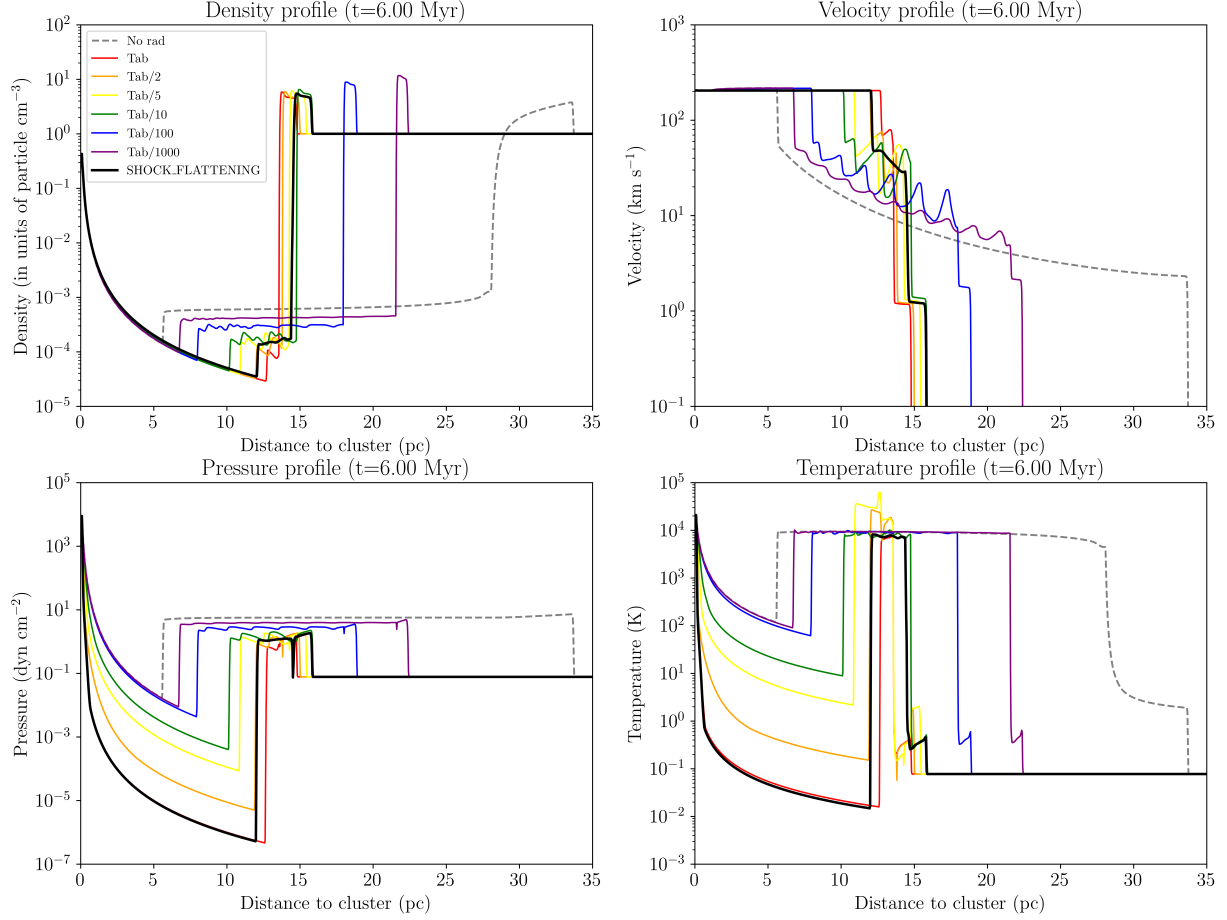


Figure 2.7: Results for the radial profiles obtained by decreasing emission rates. The simulation with the SHOCK_FLATTENING subroutine has been added to the plot and shows a much more physical behaviour than the others. Initial conditions and parameters are detailed in Section 2.2.

treatment when strong shocks and steep gradients are present.

From a physical perspective, the influence of radiative cooling becomes evident as the cooling intensity increases. The shocked wind bubble progressively shrinks and eventually almost disappears in the strongest cooling cases, resulting in a configuration that transitions nearly directly from the free wind to the shocked ISM. This is a significant qualitative change in the structure of the system. Compared with the fiducial purely hydrodynamical simulation (shown in dashed gray), the size of the bubble is notably reduced and the shell is considerably thinner. This behaviour is in good agreement with observational evidence, which reports bubble sizes smaller than those predicted by Weaver’s model. Therefore, these results reinforce the idea that radiative cooling is a crucial ingredient in obtaining realistic stellar wind bubble

models.

2.3.4 Application to real star cluster

To conclude this section, we present a set of simulations based on the physical parameters of the young massive stellar cluster M16 (also known as the Eagle Nebula). This system provides an interesting test case due to its well-characterized properties and the availability of observational constraints. We ran three distinct simulations: a purely hydrodynamical one, a second that included thermal conduction and a third incorporating both conduction and radiative cooling. This progression allows us to assess how each additional physical process modifies the evolution of the bubble and how closely the numerical results approximate the observed structure of M16. The Figure 2.8 shows the results for all these runs.

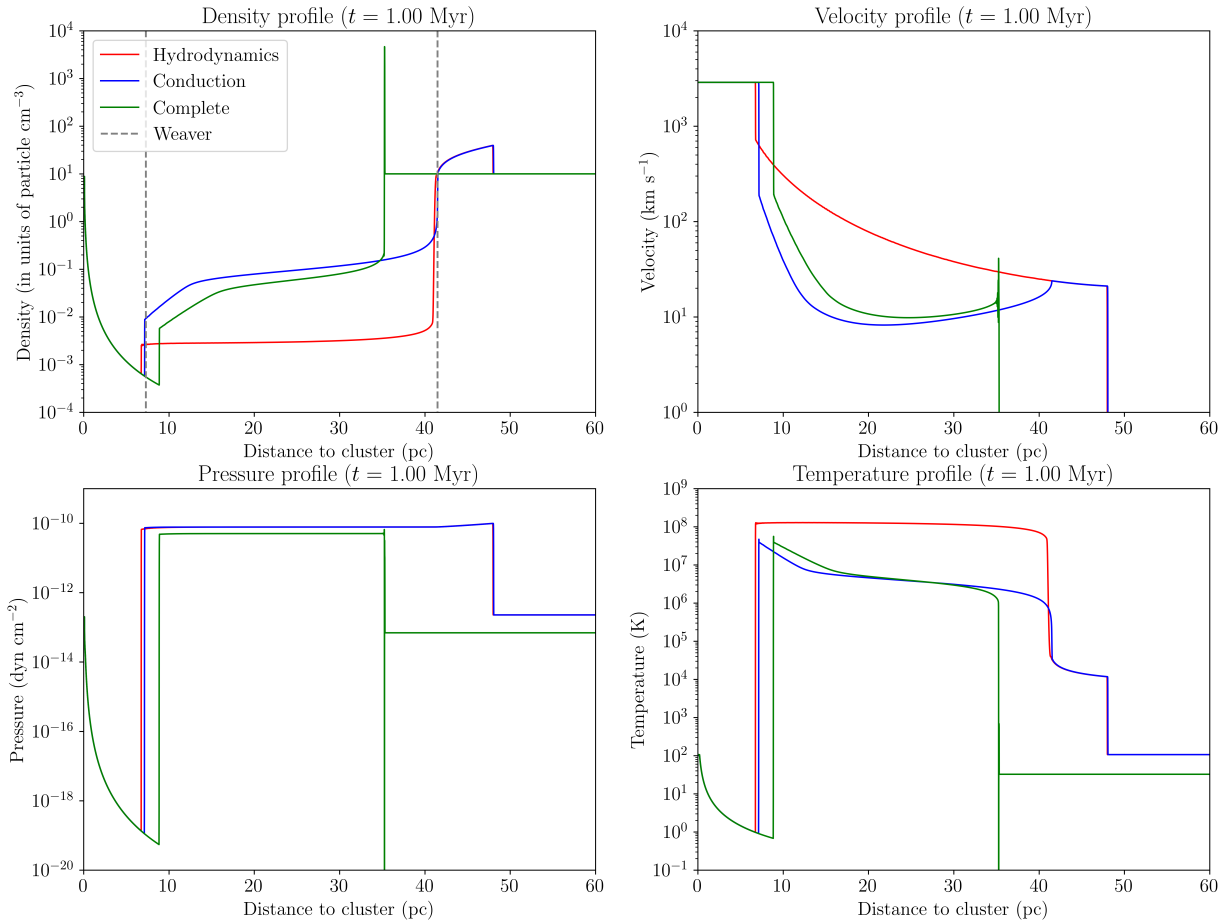


Figure 2.8: Results for the radial profiles obtained by different physical models, using M16 parameters as initial condition [55].

Although the estimated age of M16 is estimated to be around ~ 2 Myr, we find that even when simulating only up to 1 Myr, the predicted bubble radius exceeds the observed one ($R_{\text{obs}}^{\text{M16}} \simeq 10$ [56, 57]) in all cases (including the most physically complete model with radiative cooling). This discrepancy highlights the limitations of one-dimensional simulations, which cannot capture the development of multidimensional hydrodynamical and magnetohydrodynamical instabilities that are known to strongly influence bubble evolution. Nonetheless, the simulation with conduction and radiation yields a significantly better agreement with observations than simpler models and, in particular, improves the predictions of the Weaver solution. This is especially relevant considering that the Weaver model tends to overestimate bubble sizes due to its neglect of radiative losses and geometric instabilities, which are only partially included in our one-dimensional treatment.

It is also worth noting that, in order to properly resolve the extremely thin shell forming at the edge of the bubble, we increased the spatial resolution up to 25000 grid points in the case of the complete simulation. This level of refinement was necessary to fully capture the structure of the shell without introducing numerical artifacts. What is remarkable is that, thanks to the reduced dimensionality of the model, the simulations remained computationally feasible despite the high resolution.

The formation of a very dense and compact shell (almost resembling a Dirac delta) is not an anomaly, but rather a well-understood and expected feature of these systems. Physically, the dynamics within the bubble shell lead to the accumulation of material and compression at the shock front, which in turn increases the efficiency of radiative cooling. This enhanced cooling causes further contraction, reinforcing the shell's thin and dense profile. Such behaviour has been documented in previous studies [58, 59], where it posed significant numerical challenges, especially in multidimensional simulations. In our case, while the use of a one dimensional framework reduced computational difficulties, we did encounter calculations limitations for certain parameter regimes.

Finally, it is interesting to note that in the hydrodynamical and conduction-only cases, the positions of the contact discontinuity and the termination shock predicted by our simulations match remarkably well with those obtained analytically from the Weaver solution (not only for M16, but also for other clusters tested). However, once radiative cooling is included, deviations appear, as expected, reinforcing the idea that radiation plays a critical role in shaping the observable structure of stellar wind bubbles.

With this, we have achieved the intended objectives regarding the numerical simulation of

the stellar wind bubble, obtaining physically consistent and sufficiently detailed radial profiles for the main dynamical quantities. These results lay the foundation for the next stage of the project, which consists in implementing a solver for the cosmic ray transport equation. The output of PLUTO simulations analogous to the presented in this section will serve as input profiles for this following transport model in future works.

Chapter 3

Development of a numerical solver for transport equation

3.1 Mathematical foundations of the solver

We now present the main aspects of the mathematical derivation regarding the design of the numerical solver developed in this work. The objective is to solve the transport problem formulated in equation (1.7), which describes the time evolution of the cosmic ray distribution function $f(t, r, p)$ under spherical symmetry. As discussed in the previous section, this equation includes advection, diffusion, adiabatic losses and source injection terms, and must be solved over a finite radial domain with physically motivated boundary and initial conditions.

To the best of our knowledge, no publicly available numerical code currently solves this equation in spherical coordinates with the required level of generality and in a form adapted to wind-blown bubble environments. Existing high-quality tools such as GALPROP [24], DRAGON [25] and PICARD [26] are primarily designed for different contexts (large-scale galactic cosmic ray transport) and operate in cartesian or cylindrical geometries. Nonetheless, some of their algorithmic structures and numerical strategies have served as useful reference points during the design phase of our solver. Although the physical problem and mathematical structure solved here are different, some specific implementation decisions have been inspired by the general logic of those well-established frameworks. It is important to stress, however, that all the mathematical formulation and numerical derivation presented in the following sections have been developed independently as part of this thesis work.

First of all, it is important to talk about the discretization of the spatial and temporal domain.

Let us remind that $t \in [0, t_{\text{end}}]$, $r \in [0, R_{\text{end}}]$ and $p \in [0, p_{\text{max}}]$. Now, the discretization is done as follows:

1. Time will be divided in $N_t + 1$ points such that $t \in \{t_0, t_1, \dots, t_{N_t}\}$. In particular, we are considering $t_0 = 0$.
2. Regarding radial coordinate, we apply an static and homogeneous discretization so as to use $N_r + 2$ points, thus $r \in \{r_0, r_1, \dots, r_{N_r}, r_{N_r+1}\}$. This way, $r_0 = 0$ y $r_{N_r+1} = R_B$ are fixed by boundary conditions.
3. For the momentum coordinate we proceed in an analogous way so as to have $p \in \{p_0, \dots, p_{N_p}\}$.

This discretization¹ implies that each node of simulation is uniquely determined by 3 indexes: n, i, k . Index n refers to time t_n ; index i to position r_i ; and index k to momentum p_k . Under these conditions we can make use of the notation $f_{ik}^n \equiv f(t_n, r_i, p_k)$.

We will now focus purely on the numerical methodology used. A widely used strategy for the numerical solution of partial differential equations (PDEs) is the so-called *operator splitting method*. In this approach, the PDE (typically composed of several distinct operators) is treated as a superposition of independent subproblems. That is, in our case,

$$\frac{\partial f}{\partial t} = \sum_{\alpha} \mathcal{L}_{\alpha} + Q,$$

where $\alpha \in \{D, P, A\}$ refers to the advection, momentum loss and diffusion operators, respectively.

As previously discussed, in our case these operators take the form

$$\begin{cases} \mathcal{L}_D = \frac{1}{r^2} \frac{\partial}{\partial r} \left(r^2 D \frac{\partial f}{\partial r} \right) = \frac{2D}{r} \frac{\partial f}{\partial r} + \frac{\partial}{\partial r} \left(D \frac{\partial f}{\partial r} \right) = \left(\frac{2D}{r} + \frac{\partial D}{\partial r} \right) \frac{\partial f}{\partial r} + D \frac{\partial^2 f}{\partial r^2}, \\ \mathcal{L}_P = \frac{\partial}{\partial p} \left[\frac{p}{3} \left(\frac{1}{r^2} \frac{\partial(r^2 u_r)}{\partial r} \right) f \right], \\ \mathcal{L}_A = -\frac{1}{r^2} \frac{\partial(r^2 u_r f)}{\partial r}. \end{cases}$$

The idea behind the method is to advance the solution in time by applying each operator successively. To illustrate this, using the notation previously mentioned, let us see what the procedure to compute f^{n+1} is

¹It is worth mentioning here that, in the specific implementation to be carried out in future work, where the results from PLUTO simulations will be used, the discretization employed by this solver will be related to the resolution used by PLUTO. However, a detailed discussion of this aspect falls outside the scope of the current development and will not be addressed at this stage.

1. We first define an intermediate solution, f^* , as the solution to

$$\frac{\partial f^*}{\partial t} = \mathcal{L}_D(f^*) + \frac{Q}{3}$$

over the interval $t \in [t_n, t_{n+1}]$, with the initial condition $f^*(t_n, \cdot, \cdot) = f^n$.

2. The resulting $f^*(t_{n+1}, \cdot, \cdot)$ is then used as the initial condition for the next subproblem. The second intermediate solution, f^{**} , is obtained by solving

$$\frac{\partial f^{**}}{\partial t} = \mathcal{L}_P(f^{**}) + \frac{Q}{3}$$

over the same interval $t \in [t_n, t_{n+1}]$, with $f^{**}(t_n, \cdot, \cdot) = f^*(t_{n+1}, \cdot, \cdot)$.

3. Similarly, a third intermediate step is considered by solving

$$\frac{\partial f^{***}}{\partial t} = \mathcal{L}_A(f^{***}) + \frac{Q}{3},$$

again over $t \in [t_n, t_{n+1}]$, with the initial condition $f^{***}(t_n, \cdot, \cdot) = f^{**}(t_{n+1}, \cdot, \cdot)$.

4. Finally, the updated solution at the next time step is defined as the result of this successive application of operators: $f^{n+1} = f^{***}(t_{n+1}, \cdot, \cdot)$.

This strategy offers several advantages. For instance, each subproblem can be advanced in time with its own dedicated time-stepping scheme, allowing for local refinement depending on the precision requirements of each operator. Furthermore, the numerical treatment of each term can be addressed individually, without being constrained by the discretization of the other terms. This flexibility enables the construction of highly modular and general-purpose solvers, which can be adapted to include only the physical processes relevant to a given problem².

Regarding the specific order of implementation of operators in the operator splitting scheme, specific investigation is needed to determine what the optimal setup is for our specific purposes. Such analysis is left for a subsequent work focused on the case of use of our solver.

In what follows, we present the numerical treatment of each of the 3 subproblems relevant to our study.

²In such scenarios, for each substep in the time evolution, the source term Q must be divided by n_{Op} , the number of operators being split. In our particular case, we have $n_{Op} = 3$.

3.1.1 Diffusion operator

For the diffusive subproblem in our operator splitting approach, the goal is to solve the system

$$\begin{cases} \frac{\partial f}{\partial t} = \frac{1}{r^2} \frac{\partial}{\partial r} \left(r^2 D \frac{\partial f}{\partial r} \right) + \frac{Q}{3}, \\ \frac{\partial f}{\partial r}(t, 0, \cdot) = 0, \quad f(t, R_{\text{end}}, \cdot) = f_{\text{ISM}}(\cdot), \\ f(0, r, \cdot) = f_{\text{Inj}}(\cdot) \delta(r - R_{\text{TS}}), \end{cases}$$

within the discretized spatial domain. This operator presents a particular challenge that becomes evident when the PDE is rewritten in the expanded form,

$$\frac{\partial f}{\partial t} = \left(\frac{2D}{r} + \frac{\partial D}{\partial r} \right) \frac{\partial f}{\partial r} + D \frac{\partial^2 f}{\partial r^2} + \frac{Q}{3}.$$

A singularity arises at $r = 0$. However, applying L'Hôpital's rule allows us to establish that

$$\lim_{r \rightarrow 0} \frac{2D}{r} \frac{\partial f}{\partial r} = \lim_{r \rightarrow 0} 2 \left(\frac{\partial D}{\partial r} \frac{\partial f}{\partial r} + D \frac{\partial^2 f}{\partial r^2} \right).$$

This implies that, at $r \rightarrow 0$, the equation becomes

$$\lim_{r \rightarrow 0} \frac{\partial f}{\partial t} = 3 \left(\frac{\partial D}{\partial r} \frac{\partial f}{\partial r} + D \frac{\partial^2 f}{\partial r^2} \right) + \frac{Q}{3} = 3D \frac{\partial^2 f}{\partial r^2} + \frac{Q}{3},$$

where we have used the necessary symmetry condition in spherical coordinates, $\frac{\partial f}{\partial r}(t, 0, \cdot) = 0$.

The discretization of the diffusion operator at $r = 0$ is straightforward (and equivalent to the cartesian case). In particular, using the Crank–Nicolson method, we obtain

$$\begin{aligned} \frac{f_0^{n+1} - f_0^n}{\Delta t} = & 3 \left[\frac{1}{2} \left(D_0^{n+1} \frac{f_1^{n+1} - 2f_0^{n+1} + f_{-1}^{n+1}}{(\Delta r)^2} \right) + \frac{1}{2} \left(D_0^n \frac{f_1^n - 2f_0^n + f_{-1}^n}{(\Delta r)^2} \right) \right] \\ & + \frac{1}{3} \left[\frac{1}{2} Q_0^{n+1} + \frac{1}{2} Q_0^n \right]. \end{aligned}$$

Moreover, by symmetry, we have $f_{-1} = f_1$, so the expression simplifies to

$$\frac{f_0^{n+1} - f_0^n}{\Delta t} = 3 \left[\left(D_0^{n+1} \frac{f_1^{n+1} - f_0^{n+1}}{(\Delta r)^2} \right) + \left(D_0^n \frac{f_1^n - f_0^n}{(\Delta r)^2} \right) \right] + \frac{1}{3} \left[\frac{1}{2} Q_0^{n+1} + \frac{1}{2} Q_0^n \right].$$

Inside the domain, for a generic node i , the discretization of the original equation yields

$$\begin{aligned} \frac{f_i^{n+1} - f_i^n}{\Delta t} = & \left[\frac{1}{2} \left(\frac{2D_i^{n+1}}{r_0 + i\Delta r} + \frac{D_{i+1}^{n+1} - D_{i-1}^{n+1}}{2\Delta r} \right) \left(\frac{f_{i+1}^{n+1} - f_{i-1}^{n+1}}{2\Delta r} \right) \right. \\ & + \frac{1}{2} \left(\frac{2D_i^n}{r_0 + i\Delta r} + \frac{D_{i+1}^n - D_{i-1}^n}{2\Delta r} \right) \left(\frac{f_{i+1}^n - f_{i-1}^n}{2\Delta r} \right) \Big] \\ & + \left[\frac{1}{2} \left(D_i^{n+1} \frac{f_{i+1}^{n+1} - 2f_i^{n+1} + f_{i-1}^{n+1}}{(\Delta r)^2} \right) + \frac{1}{2} \left(D_i^n \frac{f_{i+1}^n - 2f_i^n + f_{i-1}^n}{(\Delta r)^2} \right) \right] \\ & + \frac{1}{3} \left[\frac{1}{2} Q_i^{n+1} + \frac{1}{2} Q_i^n \right]. \end{aligned}$$

Rearranging both sides leads to

$$\begin{aligned} \frac{f_i^{n+1}}{\Delta t} - \frac{1}{2} \left(\frac{2D_i^{n+1}}{r_0 + i\Delta r} + \frac{D_{i+1}^{n+1} - D_{i-1}^{n+1}}{2\Delta r} \right) \left(\frac{f_{i+1}^{n+1} - f_{i-1}^{n+1}}{2\Delta r} \right) - \frac{1}{2} \left(D_i^{n+1} \frac{f_{i+1}^{n+1} - 2f_i^{n+1} + f_{i-1}^{n+1}}{(\Delta r)^2} \right) - \frac{1}{6} Q_i^{n+1} = \\ \frac{f_i^n}{\Delta t} + \frac{1}{2} \left(\frac{2D_i^n}{r_0 + i\Delta r} + \frac{D_{i+1}^n - D_{i-1}^n}{2\Delta r} \right) \left(\frac{f_{i+1}^n - f_{i-1}^n}{2\Delta r} \right) + \frac{1}{2} \left(D_i^n \frac{f_{i+1}^n - 2f_i^n + f_{i-1}^n}{(\Delta r)^2} \right) + \frac{1}{6} Q_i^n. \end{aligned}$$

As usual, we now define the coefficients

$$s_i^n = \frac{\Delta t}{4\Delta r} \left(\frac{2D_i^n}{r_0 + i\Delta r} + \frac{D_{i+1}^n - D_{i-1}^n}{2\Delta r} \right) \quad \text{and} \quad q_i^n = \frac{\Delta t D_i^n}{2(\Delta r)^2};$$

and the expression can then be rewritten as

$$\begin{aligned} f_i^{n+1} - s_i^{n+1} (f_{i+1}^{n+1} - f_{i-1}^{n+1}) - q_i^{n+1} (f_{i+1}^{n+1} - 2f_i^{n+1} + f_{i-1}^{n+1}) - \frac{\Delta t}{6} Q_i^{n+1} = \\ f_i^n + s_i^n (f_{i+1}^n - f_{i-1}^n) + q_i^n (f_{i+1}^n - 2f_i^n + f_{i-1}^n) + \frac{\Delta t}{6} Q_i^n. \end{aligned}$$

Finally, by separating the terms at times $n+1$ and n , we obtain the desired formulation

$$\begin{aligned} (s_i^{n+1} - q_i^{n+1}) f_{i-1}^{n+1} + (1 + 2q_i^{n+1}) f_i^{n+1} - (s_i^{n+1} + q_i^{n+1}) f_{i+1}^{n+1} - \frac{\Delta t}{6} Q_i^{n+1} = \\ -(s_i^n - q_i^n) f_{i-1}^n + (1 - 2q_i^n) f_i^n + (s_i^n + q_i^n) f_{i+1}^n + \frac{\Delta t}{6} Q_i^n. \end{aligned}$$

An analogous treatment can be applied to the equation at $r = 0$, for which we first define

$$q_0^n = \frac{3D_0^n \Delta t}{(\Delta r)^2}.$$

After some algebra, we arrive at the final system

$$\begin{cases} (1 + q_0^{n+1}) f_0^{n+1} - q_0^{n+1} f_1^{n+1} - \frac{\Delta t}{6} Q_0^{n+1} = (1 - q_0^n) f_0^n + q_0^n f_1^n + \frac{\Delta t}{6} Q_0^n \\ (s_i^{n+1} - q_i^{n+1}) f_{i-1}^{n+1} + (1 + 2q_i^{n+1}) f_i^{n+1} - (s_i^{n+1} + q_i^{n+1}) f_{i+1}^{n+1} - \frac{\Delta t}{6} Q_i^{n+1} = \\ \quad -(s_i^n - q_i^n) f_{i-1}^n + (1 - 2q_i^n) f_i^n + (s_i^n + q_i^n) f_{i+1}^n + \frac{\Delta t}{6} Q_i^n. \end{cases}$$

It is common to write the Crank–Nicolson system in matrix form. To do so, we define the

matrices

$$\tilde{A}^{n+1} = \begin{pmatrix} 1 + q_0^{n+1} & -q_0^{n+1} & 0 & 0 & 0 & \dots & 0 \\ s_1^{n+1} - q_1^{n+1} & 1 + 2q_1^{n+1} & -s_1^{n+1} - q_1^{n+1} & 0 & 0 & \dots & 0 \\ 0 & s_2^{n+1} - q_2^{n+1} & 1 + 2q_2^{n+1} & -s_2^{n+1} - q_2^{n+1} & 0 & \dots & 0 \\ 0 & 0 & s_3^{n+1} - q_3^{n+1} & 1 + 2q_3^{n+1} & -s_3^{n+1} - q_3^{n+1} & \dots & 0 \\ \vdots & \vdots & \vdots & \ddots & \ddots & \ddots & \vdots \\ 0 & 0 & 0 & \dots & s_{N_r-1}^{n+1} - q_{N_r-1}^{n+1} & 1 + 2q_{N_r-1}^{n+1} & -s_{N_r-1}^{n+1} - q_{N_r-1}^{n+1} \\ 0 & 0 & 0 & \dots & 0 & s_{N_r}^{n+1} - q_{N_r}^{n+1} & 1 + 2q_{N_r}^{n+1} \end{pmatrix}$$

and

$$A^n = \begin{pmatrix} 1 - q_0^n & q_0^n & 0 & 0 & 0 & \dots & 0 \\ q_1^n - s_1^n & 1 - 2q_1^n & s_1^n + q_1^n & 0 & 0 & \dots & 0 \\ 0 & q_2^n - s_2^n & 1 - 2q_2^n & s_2^n + q_2^n & 0 & \dots & 0 \\ 0 & 0 & q_3^n - s_3^n & 1 - 2q_3^n & s_3^n + q_3^n & \dots & 0 \\ \vdots & \vdots & \vdots & \ddots & \ddots & \ddots & \vdots \\ 0 & 0 & 0 & \dots & q_{N_r-1}^n - s_{N_r-1}^n & 1 - 2q_{N_r-1}^n & s_{N_r-1}^n + q_{N_r-1}^n \\ 0 & 0 & 0 & \dots & 0 & q_{N_r}^n - s_{N_r}^n & 1 - 2q_{N_r}^n \end{pmatrix}.$$

Hence, the full system of equations can be written as

$$\tilde{A}^{n+1} F^{n+1} + U_{\text{cc}}^{n+1} - \frac{\Delta t}{6} Q^{n+1} = A^n F^n + U_{\text{cc}}^n + \frac{\Delta t}{6} Q^n,$$

where $\tilde{U}_{\text{cc}}^{n+1}$ and U_{cc}^n contain non-zero components only in the last entry, encoding the boundary condition at R_{N_r+1} .

Therefore, the solution at time $n + 1$ is given by

$$F^{n+1} = \left(\tilde{A}^{n+1} \right)^{-1} \left(A^n F^n + U_{\text{cc}}^n - \tilde{U}_{\text{cc}}^{n+1} + \frac{\Delta t}{6} (Q^n + Q^{n+1}) \right).$$

3.1.2 Loss operator

Once we have treated the diffusion operator, let us focus on the loss subproblem. Firstly, it is worth noting that the loss operator can be rewritten with the form

$$\frac{\partial f}{\partial t} = -\frac{\partial}{\partial p} [\dot{P}f] + \frac{Q}{3}.$$

Here we adopt the notation $\dot{P} = \dot{P}(t, r, p)$ to denote the momentum loss rate. Since these losses act by shifting the entire spectrum toward lower momenta (this is, reducing the population at higher p in favor of lower p values), it is appropriate to employ an *upwind* discretization scheme. This is, we can take advantage of the physical direction of propagation in the system, using only the upstream values (e.g., f_k^n and f_{k+1}^n) to compute f_k^{n+1} , since information from f_{k-1}^{n-1} does not influence the solution at higher momenta. Specifically, we also apply a temporal averaging to remain consistent with the Crank–Nicolson approach, such that we consider the following discretization

$$\left(\frac{\partial f}{\partial t}\right)_{k+\frac{1}{2}}^{n+\frac{1}{2}} = \left(-\frac{\partial}{\partial p} [\dot{P}f]\right)_{k+\frac{1}{2}}^{n+\frac{1}{2}} + \left(\frac{Q}{3}\right)_{k+\frac{1}{2}}^{n+\frac{1}{2}}.$$

By developing the appropriate finite difference expressions, one arrives at the following relation

$$\begin{aligned} \frac{1}{2} \left[\left(\frac{\partial f}{\partial t}\right)_{k+1}^{n+\frac{1}{2}} + \left(\frac{\partial f}{\partial t}\right)_k^{n+\frac{1}{2}} \right] &= -\frac{1}{2} \left[\left(\frac{\partial}{\partial p} [\dot{P}f]\right)_{k+\frac{1}{2}}^{n+1} + \left(\frac{\partial}{\partial p} [\dot{P}f]\right)_{k+\frac{1}{2}}^n \right] + \left(\frac{Q}{3}\right)_{k+\frac{1}{2}}^{n+\frac{1}{2}} \\ \Rightarrow \left(\frac{f_k^{n+1} - f_k^n}{\Delta t}\right) + \left(\frac{f_{k+1}^{n+1} - f_{k+1}^n}{\Delta t}\right) &= -\left(\frac{\dot{P}_{k+1}^{n+1} f_{k+1}^{n+1} - \dot{P}_k^{n+1} f_k^{n+1}}{\Delta p}\right) + \left(\frac{\dot{P}_{k+1}^n f_{k+1}^n - \dot{P}_k^n f_k^n}{\Delta p}\right) + 2\left(\frac{Q}{3}\right)_{k+\frac{1}{2}}^{n+\frac{1}{2}}. \end{aligned}$$

Rearranging the terms and multiplying both sides by Δt , the expression simplifies to

$$\left(1 - \frac{\dot{P}_k^{n+1} \Delta t}{\Delta p}\right) f_k^{n+1} + \left(1 + \frac{\dot{P}_{k+1}^{n+1} \Delta t}{\Delta p}\right) f_{k+1}^{n+1} = \left(1 + \frac{\dot{P}_k^n \Delta t}{\Delta p}\right) f_k^n + \left(1 - \frac{\dot{P}_{k+1}^n \Delta t}{\Delta p}\right) f_{k+1}^n + 2\Delta t \left(\frac{Q}{3}\right)_{k+\frac{1}{2}}^{n+\frac{1}{2}}.$$

At this point, we can define a helpful constant,

$$d_k^n = -\frac{\dot{P}_k^n \Delta t}{\Delta p},$$

which leads to a more compact form of the system:

$$(1 + d_k^{n+1}) f_k^{n+1} + (1 - d_{k+1}^{n+1}) f_{k+1}^{n+1} = (1 - d_k^n) f_k^n + (1 + d_{k+1}^n) f_{k+1}^n + 2\Delta t \left(\frac{Q}{3}\right)_{k+\frac{1}{2}}^{n+\frac{1}{2}}.$$

It is worth noting that in this case, the point $k = 0$ does not pose any difficulties and the general update rule can be applied directly. However, for $k = N_p$, a boundary condition must be

imposed. A reasonable and convenient assumption is to choose a momentum range wide enough so that $f_{N_p+1} = 0$, which allows us to write

$$\left(1 + d_{N_p}^{n+1}\right) f_{N_p}^{n+1} = \left(1 - d_{N_p}^n\right) f_{N_p}^n + 2\Delta t \left(\frac{Q}{3}\right)_{N_p+\frac{1}{2}}^{n+\frac{1}{2}}.$$

Under these conditions, we can define the following matrices

$$\tilde{B}^{n+1} = \begin{pmatrix} 1 + d_0^{n+1} & 1 - d_1^{n+1} & 0 & 0 & \cdots & 0 \\ 0 & 1 + d_1^{n+1} & 1 - d_2^{n+1} & 0 & \cdots & 0 \\ 0 & 0 & 1 + d_2^{n+1} & 1 - d_3^{n+1} & \cdots & 0 \\ \vdots & \vdots & \vdots & \ddots & \ddots & \vdots \\ 0 & 0 & 0 & \cdots & 1 + d_{N_p-1}^{n+1} & 1 - d_{N_p}^{n+1} \\ 0 & 0 & 0 & \cdots & 0 & 1 + d_{N_p}^{n+1} \end{pmatrix}$$

and

$$B^n = \begin{pmatrix} 1 - d_0^n & 1 + d_1^n & 0 & 0 & \cdots & 0 \\ 0 & 1 - d_1^n & 1 + d_2^n & 0 & \cdots & 0 \\ 0 & 0 & 1 - d_2^n & 1 + d_3^n & \cdots & 0 \\ \vdots & \vdots & \vdots & \ddots & \ddots & \vdots \\ 0 & 0 & 0 & \cdots & 1 - d_{N_p-1}^n & 1 + d_{N_p}^n \\ 0 & 0 & 0 & \cdots & 0 & 1 - d_{N_p}^n \end{pmatrix};$$

and, thus, the system can finally be written in matrix form as

$$\tilde{B}^{n+1} F^{n+1} = B^n F^n + \frac{2\Delta t}{3} Q.$$

In conclusion, the solution at the next time step is obtained through

$$F^{n+1} = \left(\tilde{B}^{n+1}\right)^{-1} \left(B^n F^n + \frac{2\Delta t}{3} Q\right).$$

3.1.3 Advection operator

We now turn to the treatment of the advective term in the transport equation. From a mathematical and numerical perspective, the development is analogous to that of the loss

operator presented in the previous section. In particular, since we are assuming that the radial velocity field $u_r > 0$, it is justified and numerically appropriate to apply again an *upwind* discretization scheme. This choice guarantees stability and physical consistency, as the characteristics of the equation propagate from smaller to larger values of the radial coordinate.

The main structural difference with respect to the previous case lies in the indexing of the discretization. While in the loss term the population shifted from higher to lower momentum bins (thus, making use of indices k and $k+1$), the advection operator shifts the solution in space from lower to higher radial positions. Therefore, the derivation will now involve the nodes $i-1$ and i , reflecting the downstream direction of propagation.

Let us recall that the advection subproblem is based on the equation

$$\frac{\partial f}{\partial t} = -\frac{1}{r^2} \frac{\partial(r^2 u_r f)}{\partial r} + \frac{Q}{3}.$$

Before showing the numerical approximations, it is important to note that we come to a problem in $r = 0$, just as it happened in the diffusion term. We can, however, take the limit to see that

$$\lim_{r \rightarrow 0} \frac{\partial f}{\partial t} = \lim_{r \rightarrow 0} -\frac{1}{r^2} \frac{\partial(r^2 u_r f)}{\partial r} + \frac{Q}{3} = \lim_{r \rightarrow 0} -\frac{1}{r^2} \left(2r u_r f + r^2 \frac{\partial(u_r f)}{\partial r} \right) + \frac{Q}{3} = -\left. \frac{\partial(u_r f)}{\partial r} \right|_{r=0} + \frac{Q}{3} \Big|_{r=0};$$

if we assume that $u_r f$ is finite at $r = 0$, which is the case we are interested in. Of course, for our purposes, $u_r f$ will, in particular, be sufficiently smooth at $r = 0$ so as to consider that the spatial first derivative vanishes. This is to say,

$$\lim_{r \rightarrow 0} \frac{\partial f}{\partial t} = \frac{Q}{3} \Big|_{r=0}.$$

Moreover, for the purposes of our solver, $Q|_{r=0} = 0$, so the value $f(t, 0)$ is conserved for $t > 0$. This may seem counterintuitive, as even when the advective velocity field u_r is non-zero, the central value of the solution appears to remain unchanged (despite the rest of the distribution being transported outwards). However, this apparent anomaly is due to the coordinate singularity in spherical symmetry at $r = 0$. In fact, this behaviour is physically reasonable: in a purely radial outflow any fluid element located exactly at the origin experiences a perfectly symmetric force balance in all directions and therefore remains stationary.

Nevertheless, such specific configurations are not expected to appear in the typical applications of our solver. Thus, it is safe to assume $f(t, 0) = 0$ as a working condition for all practical purposes.

We now move on to the numerical treatment of the advection operator. Since the derivation is analogous to the loss term, we omit the intermediate steps for the sake of brevity and to

avoid unnecessary repetition. Proceeding through the same steps of temporal averaging, upwind discretization and Crank-Nicolson scheme, we finally arrive at the following expression

$$(1 + a_i^{n+1}) f_i^{n+1} + (1 - b_{i-1}^{n+1}) f_{i-1}^{n+1} = (1 - a_i^n) f_i^n + (1 + b_{i-1}^n) f_{i-1}^n + 2\Delta t \left(\frac{Q}{3} \right)_{i-\frac{1}{2}}^{n+\frac{1}{2}}.$$

In the derivation process, we define the constants

$$a_i^n = \frac{4i^2 u_i^n \Delta t}{(2i-1)^2 \Delta r} \quad \text{and} \quad b_i^n = \frac{4i^2 u_i^n \Delta t}{(2i+1)^2 \Delta r}.$$

The discussion made for $r = 0$ simply translates to setting $f_0^n = 0$ for every n during the computation process.

This means that, in this case, the relevant matrices are

$$\tilde{C}^{n+1} = \begin{pmatrix} 0 & 0 & 0 & 0 & \cdots & 0 \\ 1 - b_0^{n+1} & 1 + a_1^{n+1} & 0 & 0 & \cdots & 0 \\ 0 & 1 - b_1^{n+1} & 1 + a_2^{n+1} & 0 & \cdots & 0 \\ \vdots & \vdots & \vdots & \ddots & \ddots & \vdots \\ 0 & 0 & 0 & \cdots & 1 + a_{N_r-1}^{n+1} & 0 \\ 0 & 0 & 0 & \cdots & 1 - b_{N_r-1}^{n+1} & 1 + a_{N_r}^{n+1} \end{pmatrix}$$

and

$$C^n = \begin{pmatrix} 0 & 0 & 0 & 0 & \cdots & 0 \\ 1 + b_0^n & 1 - a_1^n & 0 & 0 & \cdots & 0 \\ 0 & 1 + b_1^n & 1 - a_2^n & 0 & \cdots & 0 \\ \vdots & \vdots & \vdots & \ddots & \ddots & \vdots \\ 0 & 0 & 0 & \cdots & 1 - a_{N_p-1}^n & 0 \\ 0 & 0 & 0 & \cdots & 1 + b_{N_r-1}^n & 1 - a_{N_p}^n \end{pmatrix};$$

And so, in matrix formulation, the solution for the system is given by

$$F^{n+1} = \left(\tilde{C}^{n+1} \right)^{-1} \left(C^n F^n + \frac{2\Delta t}{3} Q \right).$$

3.2 Numerical validations of the solver

We have now completed the presentation of the three core routines implemented in our solver. It is therefore appropriate to move on to a set of preliminary numerical validation exercises. Naturally, the solver admits considerable potential for further optimization and more extensive validation efforts, which will need to be addressed in future works. Nonetheless, we present here the first validation runs for each of the independently derived routines.

3.2.1 Diffusion routine

To perform an initial correctness check of the routine related to the diffusive subproblem, we compare it against a case for which the analytical solution is known. Specifically, if we consider the situation where $Q(t, r) = 0$ and $D(t, r) = D$ is constant, then the problem

$$\begin{cases} \frac{\partial f}{\partial t} = \frac{1}{r^2} \frac{\partial}{\partial r} \left(r^2 D \frac{\partial f}{\partial r} \right) + \frac{Q}{3}, \\ \frac{\partial f}{\partial r}(t, 0, \cdot) = 0, \quad f(t, 1, \cdot) = 0, \\ f(0, r) = \frac{\sin(\pi r)}{2r}, \end{cases}$$

admits the analytical solution

$$f(t, r) = \frac{\sin(\pi r)}{2r} e^{-\pi^2 D t}.$$

For simplicity, we take $D = 1$ in the numerical simulations.

We can then perform a calculation with our routine using the initial condition considered and compare its temporal evolution to the one expected by the analytical expression. The results of this analysis are shown in Figure 3.1.

In the Figure, each pair of lines corresponds to a fixed time t , with colour coding indicating the time evolution. Solid lines represent the numerical solution obtained using the implemented solver, while dashed lines correspond to the exact analytical expression. The close agreement between the two confirms the correct implementation of the diffusion operator and its consistent behaviour with the Crank–Nicolson scheme used.

One of the key features visible in the plot is the exponential decay of the solution amplitude over time, which is expected from the analytical form and is accurately captured by the numerical routine. The consistency between curves is particularly notable across the entire spatial domain, including the neighbourhood of $r = 0$, where numerical schemes in spherical coordinates typically face difficulties due to the singularity. This demonstrates that the specific treatment applied at the origin is appropriate and does not lead to spurious numerical artifacts.

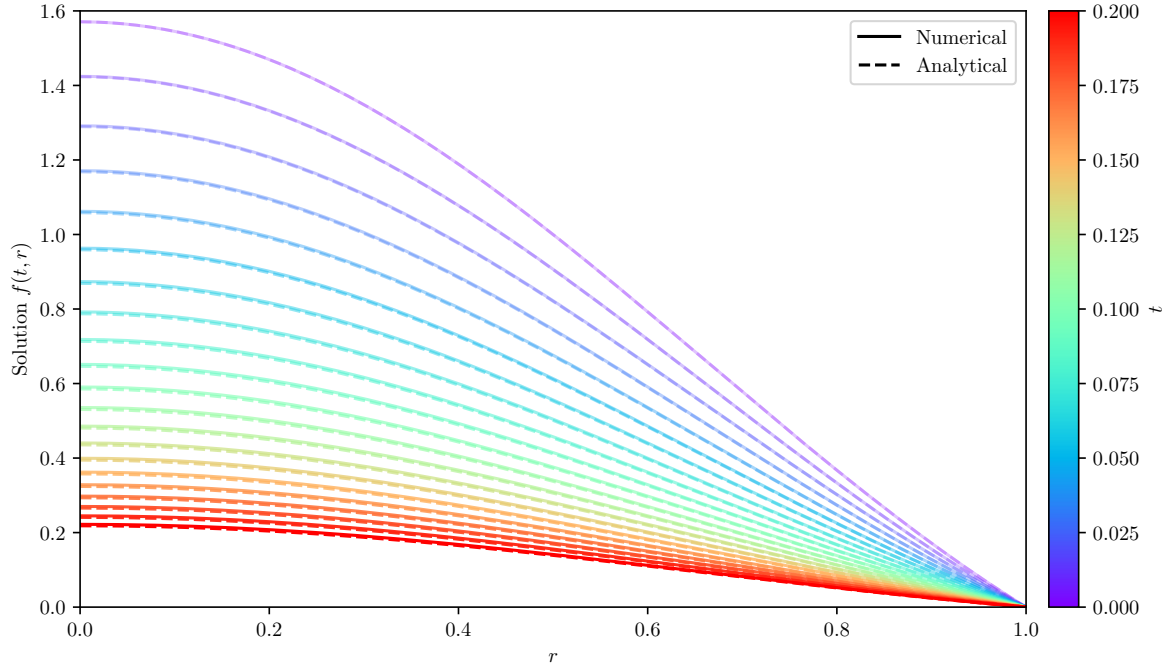


Figure 3.1: Validation of the diffusion routine. Numerical solution (solid lines) is compared with the analytical solution (dashed lines) at several time steps. The colour scale represents the evolution in time up to $t = 0.2$, with the initial condition $f(0, r) = \frac{\sin(\pi r)}{2r}$. The agreement confirms the validity of the solver for the diffusion operator in spherical geometry.

Overall, this test provides the first piece of evidence that the solver is capable of modelling the diffusion of cosmic ray populations under spherical symmetry with accuracy. It also serves as a robust foundation upon which more complex simulations involving additional transport operators can be built.

3.2.2 Loss routine

We now consider the validation of the solver in the case of losses. As described in the previous sections, the numerical routine for this operator was derived using an upwind discretization consistent with the sign of \dot{P} , combined with a Crank–Nicolson temporal averaging scheme. In order to test the correctness of this implementation, we consider a stationary state problem for which an analytical solution is known.

The idea is to check whether the numerical scheme is capable of converging towards the analytical steady state, starting from a null initial condition. More precisely, if $p \in [1, p_{\max}]$, we consider the problem

$$\begin{cases} \frac{\partial}{\partial p} [\dot{P} f] = Q, \\ f(p_{\max}) = 0, \end{cases}$$

under the assumptions

$$\begin{cases} Q = Q_0 \left(\frac{p}{p_0} \right)^{-\alpha}, \\ \dot{P} = -b_0 \left(\frac{p}{p_0} \right)^{\beta}, \end{cases}$$

where $\alpha > \beta > 0$ and $b_0, Q_0 > 0$. The source term Q injects particles at all momenta with a power-law dependence, while the momentum loss rate \dot{P} follows a similarly simple power law. These functional forms are relevant in astrophysical contexts, where radiative or adiabatic losses often scale with momentum.

Under these assumptions, the problem admits the analytical solution

$$f(p) = \frac{Q_0 p_0}{(1 - \alpha) b_0} \left[\left(\frac{p_{\max}}{p_0} \right)^{1-\alpha} \left(\frac{p}{p_0} \right)^{-\beta} - \left(\frac{p}{p_0} \right)^{1-\alpha-\beta} \right],$$

which will serve as our reference profile. Starting from the initial condition $f(0, p) = 0$, we numerically evolve the system and then compare the profile that the solution approaches with the analytical expression. This test provides a useful way to confirm that the solver handles both the shape and normalization of the spectrum correctly under the influence of continuous momentum losses.

Using $p_{\max} = 1000$, $p_0 = b_0 = Q_0 = 1$, $\alpha = 4$ and $\beta = 2$; the results of the analysis is shown in Figure 3.2.

The graphic displays the evolution of the distribution function under the sole effect of momentum losses, starting from an initial condition $f(0, p) = 0$. As time progresses, the spectrum builds up and gradually converges towards the analytical steady-state profile shown as a dashed black line. The agreement between the numerical and analytical solutions is excellent across the entire momentum range, demonstrating that the loss operator has been implemented correctly.

It is worth noting that the most significant deviations appear at early times and very low momenta. Nevertheless, the overall behaviour is robust and the numerical method successfully captures the asymptotic regime. This validation test is a first confirmation that the solver properly handles continuous losses and can be reliably used in more complex, physically motivated scenarios.

3.2.3 Advection routine

We now turn to the validation of the advection operator. As in the previous cases, we aim to compare the numerical evolution of a controlled test case with a known analytical solution in order to verify the correctness of the implementation.

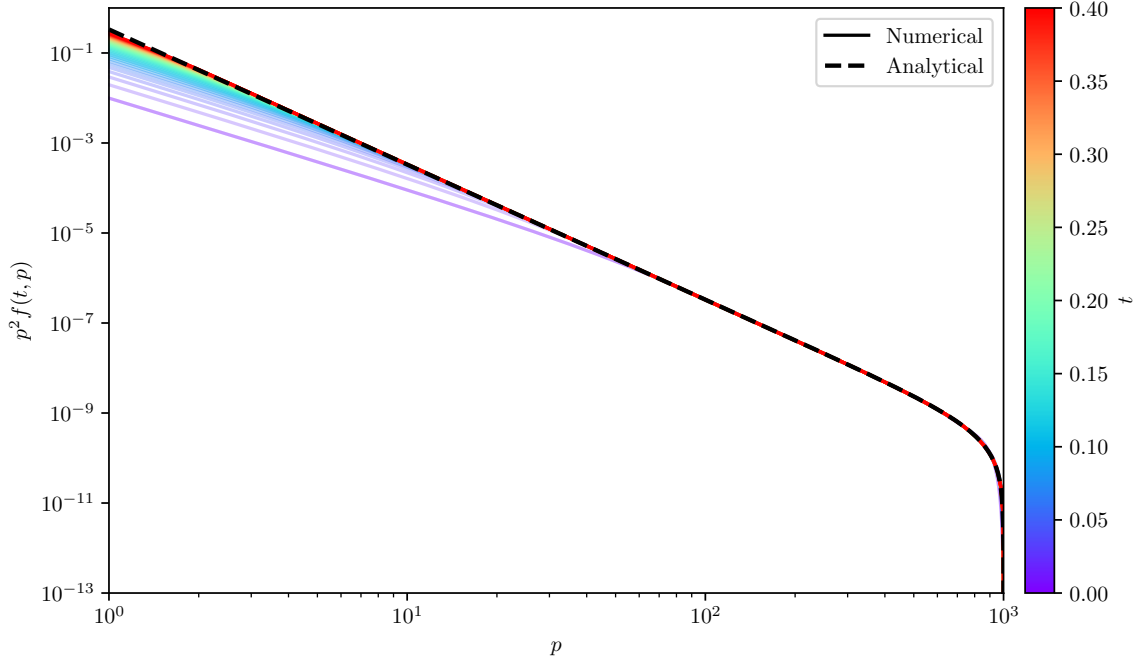


Figure 3.2: Numerical validation of the loss operator. The figure shows the temporal evolution of the spectrum $p^2 f(t, p)$ under the influence of continuous momentum losses. The solid lines correspond to the numerical solution at different times, while the dashed black line indicates the analytical steady-state solution. Momentum is shown on a logarithmic scale, and colour encodes the simulation time.

For this purpose, we consider a purely advective scenario, governed by the equation

$$\frac{\partial f}{\partial t} = -\frac{1}{r^2} \frac{\partial}{\partial r} (r^2 u_r f),$$

with a constant outward velocity field $u_r > 0$ and no source term, this is, $Q = 0$. Under these assumptions, the physical problem describes the advection of a given distribution at constant speed and the solution at any later time corresponds to a transformed initial condition. More precisely, the solution to the problem with $f(0, r) = f_0(r)$ is

$$f(t, r) = \left(\frac{r - u_r t}{r} \right)^2 f_0(r - u_r t).$$

We take as initial condition a toroidal profile in the form of a gaussian ring,

$$f(0, r) = e^{-\frac{1}{2} \left(\frac{r-0.3}{0.1} \right)^2},$$

centered at $r = 0.3$ with standard deviation of 0.1. This distribution is then transported radially outward by the wind field and we aim to recover its evolution by means of our numerical scheme. The results of the simulation are presented in Figure 3.3.

In the figure, the initial gaussian ring is transported outward under a constant radial velocity

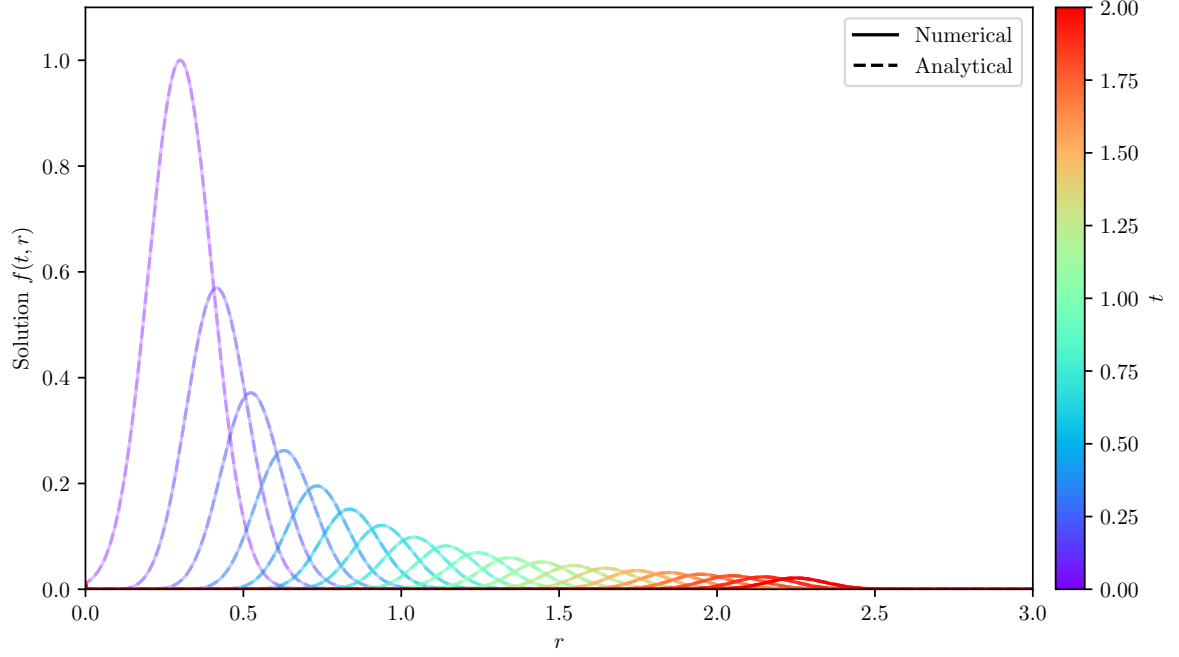


Figure 3.3: Validation of the advection routine. Numerical solution (solid lines) is compared with the analytical solution (dashed lines) at several time steps. The initial profile is a gaussian torus centered at $r = 0.3$ and is advected outward with a constant velocity field. Colour encodes time.

and the numerical solution is compared against the exact analytical expression. The excellent agreement between both confirms the accuracy of the numerical implementation.

It is important to note the progressive decay in the amplitude of the profile as time advances. This behaviour was already anticipated from the analytical solution, which includes a geometric prefactor of the form $\left(\frac{r-u_r t}{r}\right)^2$. This term arises naturally from the spherical symmetry of the problem and physically reflects the conservation of mass in a radially expanding flow. As the density moves outward, it spreads over a larger spherical surface area, leading to a dilution of the profile. The numerical results faithfully reproduce this expected behaviour, further validating the implementation of the advection routine.

This test case provides a first proof the stability and accuracy of the upwind scheme implemented for the advection operator, particularly in preserving the shape and amplitude of the transported distribution.

Conclusions

The study presented in this thesis addresses a timely and increasingly relevant question in high-energy astrophysics: the potential role of young massive star clusters as sources of cosmic rays, particularly as contributors to the population of particles reaching PeV energies. Motivated by recent observational evidence and theoretical developments, this work contributes to the field by developing numerical tools tailored to simulate the extreme environments created by the collective winds of massive stars and to study the transport of energetic particles within them.

To this end, hydrodynamical simulations of stellar wind-driven bubbles were carried out using the PLUTO code, yielding detailed spatial profiles of the relevant physical quantities that characterize the medium in which cosmic rays propagate. In parallel, a numerical solver for the spherically symmetric cosmic ray transport equation has been implemented, providing a novel computational approach adapted to the geometry and physical conditions typical of young stellar clusters. This solver, designed with computational efficiency in mind, opens the door to systematic studies and data fitting aimed at interpreting γ -ray observations.

The combination of these two components lays the foundation for a comprehensive modelling framework that bridges the gap between theoretical modelling and observational data. While this work has not included a complete analysis of observational data or cosmic ray transport simulations, it sets the stage for future developments that will allow such studies. These advancements will enable more insightful studies of individual star clusters and their potential role as γ -ray sources.

Future work will focus on integrating the solver with hydrodynamical simulations in a unified framework and providing more extensive numerical validation, exploring different cluster configurations and comparing the predicted emission with observational data. In this context, one promising extension is the incorporation of effective transport coefficients that phenomenologically account for multidimensional effects absent in 1D simulations. For instance, preliminary tests with a modified conductivity κ_{mix} , inspired by turbulent mixing

induced by hydrodynamical instabilities [60], showed encouraging qualitative results and may serve as a basis for future refinements of the model. These efforts will contribute not only to testing the PeVatron hypothesis, but also to enriching our understanding of the complex interplay between stellar evolution, plasma dynamics and particle physics in some of the most energetic environments in our galaxy.

Bibliography

- [1] Nate Bastian, Kevin R. Covey, and Michael R. Meyer. A Universal Stellar Initial Mass Function? A Critical Look at Variations. , 48:339–389, September 2010. doi: 10.1146/annurev-astro-082708-101642.
- [2] J. S. Kalirai and H. B. Richer. Star clusters as laboratories for stellar and dynamical evolution. *Philosophical Transactions of the Royal Society of London Series A*, 368(1913):755–782, January 2010. doi: 10.1098/rsta.2009.0257.
- [3] E. Vesperini. Star cluster dynamics. *Philosophical Transactions of the Royal Society of London Series A*, 368(1913): 829–849, January 2010. doi: 10.1098/rsta.2009.0260.
- [4] H. Shapley. Globular Clusters and the Structure of the Galactic System. , 30(173):42, February 1918. doi: 10.1086/122686.
- [5] E. Bica, C. Bonatto, B. Barbuy, and S. Ortolani. Globular cluster system and Milky Way properties revisited. , 450(1):105–115, April 2006. doi: 10.1051/0004-6361:20054351.
- [6] Angela Adamo, Peter Zeidler, J. M. Diederik Kruijssen, Mélanie Chevance, Mark Gieles, Daniela Calzetti, Corinne Charbonnel, Hans Zinnecker, and Martin G. H. Krause. Star Clusters Near and Far; Tracing Star Formation Across Cosmic Time. , 216(4):69, June 2020. doi: 10.1007/s11214-020-00690-x.
- [7] Roger Blandford and David Eichler. Particle acceleration at astrophysical shocks: A theory of cosmic ray origin. , 154(1):1–75, October 1987. doi: 10.1016/0370-1573(87)90134-7.
- [8] E. G. Berezhko and G. F. Krymskiĭ. REVIEWS OF TOPICAL PROBLEMS: Acceleration of cosmic rays by shock waves. *Soviet Physics Uspekhi*, 31(1):27–51, January 1988. doi: 10.1070/PU1988v031n01ABEH002534.
- [9] K. Koyama, R. Petre, E. V. Gotthelf, U. Hwang, M. Matsuura, M. Ozaki, and S. S. Holt. Evidence for shock acceleration of high-energy electrons in the supernova remnant SN1006. , 378(6554):255–258, November 1995. doi: 10.1038/378255a0.
- [10] S. P. Reynolds. Supernova remnants at high energy. , 46:89–126, September 2008. doi: 10.1146/annurev.astro.46.060407.145237.
- [11] E. A. Helder, J. Vink, A. M. Bykov, Y. Ohira, J. C. Raymond, and R. Terrier. Observational Signatures of Particle Acceleration in Supernova Remnants. , 173(1-4):369–431, November 2012. doi: 10.1007/s11214-012-9919-8.
- [12] Felix Aharonian, Ruizhi Yang, and Emma de Oña Wilhelmi. Massive stars as major factories of Galactic cosmic rays. *Nature Astronomy*, 3:561–567, March 2019. doi: 10.1038/s41550-019-0724-0.
- [13] G. Morlino, P. Blasi, E. Peretti, and P. Cristofari. Particle acceleration in winds of star clusters. , 504(4):6096–6105, July 2021. doi: 10.1093/mnras/stab690.
- [14] Zhen Cao, F. A. Aharonian, and Q. An. Ultrahigh-energy photons up to 1.4 petaelectronvolts from 12 γ -ray Galactic sources. , 594(7861):33–36, June 2021. doi: 10.1038/s41586-021-03498-z.

- [15] D. C. Abbott. The domain of radiatively driven mass loss in the H-R diagram. *Mass Loss and Evolution of O-Type Stars*, 83:237–239, January 1979.
- [16] J. P. Cassinelli. Stellar winds. , 17:275–308, January 1979. doi: 10.1146/annurev.aa.17.090179.001423.
- [17] Rolf-Peter Kudritzki and Joachim Puls. Winds from Hot Stars. , 38:613–666, January 2000. doi: 10.1146/annurev.astro.38.1.613.
- [18] M. Casse and J. A. Paul. Local gamma rays and cosmic-ray acceleration by supersonic stellar winds. , 237:236–243, April 1980. doi: 10.1086/157863.
- [19] C. J. Cesarsky and T. Montmerle. Gamma-Rays from Active Regions in the Galaxy - the Possible Contribution of Stellar Winds. , 36(2):173–193, October 1983. doi: 10.1007/BF00167503.
- [20] E. G. Klepach, V. S. Ptuskin, and V. N. Zirakashvili. Cosmic ray acceleration by multiple spherical shocks. *Astroparticle Physics*, 13(2-3):161–172, May 2000. doi: 10.1016/S0927-6505(99)00108-5.
- [21] A. Reimer, M. Pohl, and O. Reimer. Nonthermal High-Energy Emission from Colliding Winds of Massive Stars. *The Astrophysical Journal*, 644(2):1118–1144, June 2006. ISSN 0004-637X, 1538-4357. doi: 10.1086/503598. URL <https://iopscience.iop.org/article/10.1086/503598>.
- [22] Andrei M. Bykov, Alexandre Marcowith, Elena Amato, Maria E. Kalyashova, J. M. Diederik Kruijssen, and Eli Waxman. High-Energy Particles and Radiation in Star-Forming Regions. , 216(3):42, April 2020. doi: 10.1007/s11214-020-00663-0.
- [23] A. M. Bykov and I. N. Toptygin. A Model of Particle Acceleration to High Energies by Multiple Supernova Explosions in OB Associations. *Astronomy Letters*, 27(10):625–633, October 2001. doi: 10.1134/1.1404456.
- [24] A. W. Strong, I. V. Moskalenko, T. A. Porter, G. Jóhannesson, E. Orlando, and S. W. Digel. GALPROP: Code for Cosmic-ray Transport and Diffuse Emission Production. *Astrophysics Source Code Library*, record ascl:1010.028, October 2010.
- [25] Andrea Vittino, Carmelo Evoli, Daniele Gaggero, Giuseppe Di Bernardo, Mattia Di Mauro, Arianna Ligorini, Piero Ullio, and Dario Grasso. Dragon2 : A novel code for cosmic-ray transport in the galaxy. *Nuclear and Particle Physics Proceedings*, 297–299:135–142, April 2018. ISSN 2405-6014. doi: 10.1016/j.nuclphysbps.2018.07.021. URL <http://dx.doi.org/10.1016/j.nuclphysbps.2018.07.021>.
- [26] R. Kissmann. Picard: A novel code for the galactic cosmic ray propagation problem. *Astroparticle Physics*, 55: 37–50, March 2014. ISSN 0927-6505. doi: 10.1016/j.astropartphys.2014.02.002. URL <http://dx.doi.org/10.1016/j.astropartphys.2014.02.002>.
- [27] A. De Angelis. Domenico pacini, uncredited pioneer of the discovery of cosmic rays. *La Rivista del Nuovo Cimento*, 33(12):713–756, 2010. ISSN 1826-9850. doi: 10.1393/ncr/i2011-10060-9. URL <https://doi.org/10.1393/ncr/i2011-10060-9>.
- [28] Stefano Menchiari. *Probing star clusters as cosmic ray factories*. PhD thesis, Siena U., 2023.
- [29] W. R. Webber. A New Estimate of the Local Interstellar Energy Density and Ionization Rate of Galactic Cosmic Cosmic Rays. , 506(1):329–334, October 1998. doi: 10.1086/306222.
- [30] J. S. Mathis, P. G. Mezger, and N. Panagia. Interstellar radiation field and dust temperatures in the diffuse interstellar medium and in giant molecular clouds. , 128:212–229, November 1983.
- [31] R. L. Workman, V. D. Burkert, and V. Crede. Review of Particle Physics. *Progress of Theoretical and Experimental Physics*, 2022(8):083C01, August 2022. doi: 10.1093/ptep/ptac097.

- [32] Carmelo Evoli. The cosmic-ray energy spectrum, December 2020. URL <https://doi.org/10.5281/zenodo.4396125>.
- [33] L. J. Gleeson and W. I. Axford. Solar Modulation of Galactic Cosmic Rays. , 154:1011, December 1968. doi: 10.1086/149822.
- [34] Marius S. Potgieter. Solar Modulation of Cosmic Rays. *Living Reviews in Solar Physics*, 10(1):3, June 2013. doi: 10.12942/lrsp-2013-3.
- [35] D. J. Bird, S. C. Corbato, H. Y. Dai, B. R. Dawson, J. W. Elbert, B. L. Emerson, K. D. Green, M. A. Huang, D. B. Kieda, M. Luo, S. Ko, C. G. Larsen, E. C. Loh, M. H. Salamon, J. D. Smith, P. Sokolsky, P. Sommers, J. K. K. Tang, and S. B. Thomas. The Cosmic-Ray Energy Spectrum Observed by the Fly’s Eye. , 424:491, March 1994. doi: 10.1086/173906.
- [36] W. D. Apel, J. C. Arteaga-Velázquez, and K. Bekk. Ankle-like feature in the energy spectrum of light elements of cosmic rays observed with KASCADE-Grande. , 87(8):081101, April 2013. doi: 10.1103/PhysRevD.87.081101.
- [37] Kenneth Greisen. End to the Cosmic-Ray Spectrum? , 16(17):748–750, April 1966. doi: 10.1103/PhysRevLett.16.748.
- [38] Pasquale Blasi. The origin of galactic cosmic rays. , 21:70, November 2013. doi: 10.1007/s00159-013-0070-7.
- [39] J. J. Connell. Galactic Cosmic-Ray Confinement Time: Ulysses High Energy Telescope Measurements of the Secondary Radionuclide ^{10}Be . , 501(1):L59–L62, July 1998. doi: 10.1086/311437.
- [40] T. Hams, L. M. Barbier, M. Bremerich, E. R. Christian, G. A. de Nolfo, S. Geier, H. Göbel, S. K. Gupta, M. Hof, W. Menn, R. A. Mewaldt, J. W. Mitchell, S. M. Schindler, M. Simon, and R. E. Streitmatter. Measurement of the Abundance of Radioactive ^{10}Be and Other Light Isotopes in Cosmic Radiation up to 2 GeV Nucleon $^{-1}$ with the Balloon-borne Instrument ISOMAX. , 611(2):892–905, August 2004. doi: 10.1086/422384.
- [41] Bradley W. Carroll and Dale A. Ostlie. *An Introduction to Modern Astrophysics*. 1996.
- [42] B. Cameron Reed. New estimates of the solar-neighborhood massive star birthrate and the galactic supernova rate. *The Astronomical Journal*, 130(4):1652, oct 2005. doi: 10.1086/444474. URL <https://dx.doi.org/10.1086/444474>.
- [43] R. D. Blandford and J. P. Ostriker. Particle acceleration by astrophysical shocks. , 221:L29–L32, April 1978. doi: 10.1086/182658.
- [44] L. Oc. Drury. REVIEW ARTICLE: An introduction to the theory of diffusive shock acceleration of energetic particles in tenuous plasmas. *Reports on Progress in Physics*, 46(8):973–1027, August 1983. doi: 10.1088/0034-4885/46/8/002.
- [45] Pierre Cristofari. The Hunt for Pevatrons: The Case of Supernova Remnants. *Universe*, 7(9):324, August 2021. doi: 10.3390/universe7090324.
- [46] Mark R. Krumholz, Christopher F. McKee, and Joss Bland-Hawthorn. Star Clusters Across Cosmic Time. , 57: 227–303, August 2019. doi: 10.1146/annurev-astro-091918-104430.
- [47] Charles J. Lada and Elizabeth A. Lada. Embedded Clusters in Molecular Clouds. , 41:57–115, January 2003. doi: 10.1146/annurev.astro.41.011802.094844.
- [48] Simon F. Portegies Zwart, Stephen L. W. McMillan, and Mark Gieles. Young Massive Star Clusters. , 48:431–493, September 2010. doi: 10.1146/annurev-astro-081309-130834.
- [49] R. Weaver, R. McCray, J. Castor, P. Shapiro, and R. Moore. Interstellar bubbles. II. Structure and evolution. , 218: 377–395, December 1977. doi: 10.1086/155692.
- [50] L. Spitzer. *Physics of Fully Ionized Gases*. 1962.

- [51] Lachlan Lancaster, Eve C. Ostriker, Jeong-Gyu Kim, and Chang-Goo Kim. Efficiently Cooled Stellar Wind Bubbles in Turbulent Clouds. I. Fractal Theory and Application to Star-forming Clouds. , 914(2):89, June 2021. doi: 10.3847/1538-4357/abf8ab.
- [52] Lachlan Lancaster, Eve C. Ostriker, Jeong-Gyu Kim, and Chang-Goo Kim. Efficiently Cooled Stellar Wind Bubbles in Turbulent Clouds. II. Validation of Theory with Hydrodynamic Simulations. , 914(2):90, June 2021. doi: 10.3847/1538-4357/abf8ac.
- [53] A. Mignone, G. Bodo, S. Massaglia, T. Matsakos, O. Tesileanu, C. Zanni, and A. Ferrari. PLUTO: A Numerical Code for Computational Astrophysics. , 170(1):228–242, May 2007. doi: 10.1086/513316.
- [54] J M Pittard, C J Wareing, and M M Kupilas. How to inflate a wind-blown bubble. *Monthly Notices of the Royal Astronomical Society*, 508(2):1768–1776, 09 2021. ISSN 0035-8711. doi: 10.1093/mnras/stab2712. URL <https://doi.org/10.1093/mnras/stab2712>.
- [55] S. Celli, A. Specovius, S. Menchiari, A. Mitchell, and G. Morlino. Mass and wind luminosity of young Galactic open clusters in Gaia DR2. , 686:A118, June 2024. doi: 10.1051/0004-6361/202348541.
- [56] L. D. Anderson, T. M. Bania, Dana S. Balser, V. Cunningham, T. V. Wenger, B. M. Johnstone, and W. P. Armentrout. The WISE Catalog of Galactic H II Regions. , 212(1):1, May 2014. doi: 10.1088/0067-0049/212/1/1.
- [57] Stoop, M., Kaper, L., de Koter, A., Guo, D., Lamers, H. J. G. L. M., and Rieder, S. The early evolution of young massive clusters - the kinematic history of ngc 6611/m16. *AA*, 670:A108, 2023. doi: 10.1051/0004-6361/202244511. URL <https://doi.org/10.1051/0004-6361/202244511>.
- [58] Ralph S. Sutherland, David K. Bisset, and Geoffrey V. Bicknell. The numerical simulation of radiative shocks. i. the elimination of numerical shock instabilities using a local oscillation filter. *The Astrophysical Journal Supplement Series*, 147(1):187, jul 2003. doi: 10.1086/374795. URL <https://dx.doi.org/10.1086/374795>.
- [59] D. A. Badjin, S. I. Glazyrin, K. V. Manukovskiy, and S. I. Blinnikov. On physical and numerical instabilities arising in simulations of non-stationary radiatively cooling shocks. *Monthly Notices of the Royal Astronomical Society*, 459(2):2188–2211, 04 2016. ISSN 0035-8711. doi: 10.1093/mnras/stw790. URL <https://doi.org/10.1093/mnras/stw790>.
- [60] Kareem El-Badry, Eve C Ostriker, Chang-Goo Kim, Eliot Quataert, and Daniel R Weisz. Evolution of supernovae-driven superbubbles with conduction and cooling. *Monthly Notices of the Royal Astronomical Society*, 490(2):1961–1990, 10 2019. ISSN 0035-8711. doi: 10.1093/mnras/stz2773. URL <https://doi.org/10.1093/mnras/stz2773>.